What causes the persistent seismicity below the eastern flank of Piton de la Fournaise (Réunion Island)? Elasto-plastic models of magma inflation

Muriel Gerbault, Fabrice Fontaine, Aline Peltier, Jean-Luc Got, Riad Hassani, Valerie Ferrazzini, Lydie-Sarah Gailler, Zacharie Duputel

Highlights

- Seismicity at Piton de la Fournaise displays a cup shape dipping 2 km below the eastern flank's surface,
- elasto-plastic models with topographic loading and magma inflation source test various rock frictions,
- a dike-like inflation source below the eastern flank produces a too shallow dipping shear zone,
- inflation of the magma reservoir at ca. 0 km depth produces a shear zone comparable to observations,
- the 3D kinematics of this shear zone indicate that it may not spark an imminent flank slide.

What causes the persistent seismicity below the eastern flank of Piton de la Fournaise (Réunion Island) ? Elasto-plastic models of magma inflation

Muriel Gerbault[a], Fabrice J. Fontaine[b,c], Aline Peltier[b,c], Jean-Luc Got[d], Riad Hassani[e], Valerie Ferrazzini[b,c], Lydie Gailler[f], Zacharie Duputel[b,c]

[a] *IRD GET CNRS OMP 14 av. Edouard Belin 31400 Toulouse France*
[b] *Universit"'e de Paris Institut de Physique du Globe Paris CNRS F-75005 Paris France*
[c] *Observatoire volcanologique du Piton de la Fournaise F-97418 Plaine des Cafres La Runion France*
[d] *ISTERRE Universit de Savoie Chambery France*
[e] *Geoazur Universit de Nice Sophia-antipolis France*
[f] *CLERVOLC UCA Clermont-Ferrand France*

Abstract

Identifying the causes of flank destabilization of active volcanic edifices is key to prevent catastrophic events. The persistent seismicity recorded below the eastern flank of Piton de la Fournaise shield volcano (Réunion Island), both in between and during eruptive events, may give indications on the mechanical stability of this edifice. Whether this asymmetric "cup" shaped seismicity is linked to magma injections and whether it sparks a gravitational flank slide motivates this study. Here we model the elasto-plastic behavior of this volcanic edifice at crustal scale, with the 3D finite-element code Adeli. First, we test the influence of tensile failure, recently implemented in combination to a Drucker-Prager shear failure criterion; a pressurized cavity below a flat top surface triggers shear failure in general, with tensile failure restricted to the surface and cavity tip. Then we include the topography of Piton de la Fournaise in the gravity field. Considering first only elasticity, deviatoric stresses attain about 35 MPa below the volcanic edifice and displacements are maximum in the horizontal east-west direction, reaching 30 m near sea-level. Introducing plastic behavior produces a rather symmetric cup shape plastic domain around the volcano's summit, that extends at depth with reducing bedrock *effective* friction (which acts is a proxy for reduced standard friction due to pore fluid pressurization). An asymmetric listric shear zone develops down to -3 km (bsl) only if the tensile strength, cohesion and friction angle are set as low as 1.5 MPa, 3 MPa and 3°, respectively; these values hence provide a lower bound for the edifice's effective strength. The second part of this study explores the influence of an internal overpressure, which is either applied as a vertical inflation source located about 500 m below the surface of the eastern flank, simulating a distal dike, or from a deeper ellipsoid simulating the magma reservoir located at depth ca. 0 km (near sea level) below the summit. The resulting strain pattern forms a cup-shaped shear zone dipping down below the eastern flanks of the edifice, reaching depth -2 km (*bsl*) if effective friction angle is $\leq 5°$. Whereas the deep base of the dike and the eastern edge of the magma reservoir coincide geometrically in the models, the inflating dike produces a shear zone 1 km shallower than does the inflating magma reservoir, the latter coinciding better with the shape of the observed seismic cup.

Hence, we propose that this structure is a mechanical consequence of continuous magma supply in the reservoir, coherent with previous interpretations. This means that at least originally it did not need to form as a pre-existing weak zone or a magma-filled structure. However, this shear zone delimits an underlying domain in dilatation relative to a constricted hanging-wall; it may thus promote magma sills. It also branches to the surface with planar radial shear zones comparable to some observed eruptive fissures. The 3D kinematics of this shear zone does not rule out the possibility of a giant flank slide, although it does not appear today as imminent.

Keywords: volcano flankslides, elasto-plastic behavior, magma inflation, seismicity

1. Introduction

Seismicity is a common feature of active volcanoes. It results from stress changes linked to magma pressurization in reservoirs or dikes, to gravitational instabilities and to the local tectonic activity. The Piton de la Fournaise shield volcano, la Réunion Island, displays a peculiar seismic pattern in its upper most 4 km and below the Enclos Fouqué present-day caldera (Fig. **1**). This hotspot volcano produces a mean of 2 eruptions per year (Staudacher et al., 2009; Peltier et al., 2009; Roult et al., 2012) and is well monitored, making it a great natural laboratory to understand the interplay between eruption dynamics and the edifice's mechanical state. Recent eruptions are fed by a main shallow reservoir located approximately 1.5-2.5 km below the edifice's summit (Peltier et al., 2009; Di Muro et al., 2014), with magma migrating via localized dike injections that adopt vertical or inclined trajectories (e.g. Chevallier and Bachèlery, 1981; Bonali et al., 2011; Smittarello et al., 2019). Seismicity associated with these magma injections concentrates within a bulk volumetric domain about 1 to 2 km below the summit (Lengliné et al., 2016; Duputel et al., 2019, 2021). It superimposes on seismic activity in distal regions below the eastern flank of the volcano, which persists during pre-eruptive periods and bursts during magmatic intrusion events; a ca. 6 years record reveals a three-dimensional curved or *cup* shaped structure, dipping to the East down to -2 km below sea level, 5 km away from the summit (Fig. 1b, Duputel et al., 2021). Such flank seismicity has also been identified at other active volcanoes, like at Kilauea, Hawaii, where it is clearly associated with a deep tectonic decollement plane (Got et al., 1994; Poland et al., 2017). However, at Piton de la Fournaise, although N120 oriented fault lineaments have been identified consistent with regional-scale oceanic fractures (Michon et al., 2009), regional geophysical surveys (Gailler et al., 2018) and airborne MT surveys (Dumont et al., 2019) confirm that flank seismicity at Piton de la Fournaise lacks a strong control from active tectonics.

This distal, persistent seismicity in which we are interested in here, is actually observed since the installation of the first dense seismic recording network, thus since at least ca. 30 years (Hirn et al., 1991). A number of studies have explored the relation between magmatic injections patterns, surface motion and

seismicity at Piton de la Fournaise (e.g. Peltier et al., 2009; Famin and Michon, 2010; Got et al., 2013; Michon et al., 2015; Smittarello et al., 2019) indicating that this seismogenic domain may be a weakened, 'damaged' volume or/and a zone of magmatic fluid circulation or storage. The interplay between magmatic injections and the continuous motion of the eastern flank, which slips by a few cm/yr and up to tens of cm during volcanic crises (Bachèlery, 1981; Brenguier et al., 2012; Got et al., 2013; Peltier et al., 2015; Froger et al., 2015) is still debated. More than 500 km^3 of avalanche debris cover the submarine flanks of the Island (Oehler et al., 2008), which indicates regular edifice flank destabilizations and motivates the need to assess the meaning of this seismicity in terms of flank slide hazards. On the other hand, modelling studies showed the key role of edifice's strength in generating volcano flankslides, and the effect of strength reduction induced by hydrothermal fluid flow forced by magmatic injections (Iverson, 1995). However it was also shown difficult to reproduce deeply seated flankslides (at depths greater than ca. 1 km depth), because this requires extreme magma overpressure or an extremely weak decollement plane (Reid, 2004; Morgan and McGovern, 2005b; Apuani and Corazzato, 2009).

At Piton de la Fournaise and in continuity with previous studies that investigated the source(s) and the mechanical triggers of observed deformation (Cayol and Cornet, 1998; Fukushima et al., 2005, 2010; Peltier et al., 2006, 2008; Michon et al., 2009; Got et al., 2013; Tridon et al., 2016; Smittarello et al., 2019; Beauducel et al., 2020), here we explore the mechanical state of the edifice considering its crustal scale, and test whether the persistent seismicity pattern can be reproduced. Therefore we design 3D (three-dimensional) numerical models that account for the gravitational load of an edifice behaving elasto-plastic and affected by the overpressurization of a magma reservoir or a dike. While the construction of a volcanic edifice obviously results from the progressive accumulation of rock mass over hundred thousands of years by punctual magma injections, options to reproduce the appropriate stress buildup are limited (e.g. Apuani et al., 2005; Morgan and McGovern, 2005a). While one view point treats the stress field as isotropic (Cayol and Cornet, 1998), here we choose the other view point in which the edifice's topographic load is 'suddenly' imposed within the gravity field. The study aims at bracketing the potential influence on present day deformation of gravity, with and without magma pressurization, acknowledging that reciprocally, many studies have already shown how the edifice's load plays a key role in orienting the trajectory of magma towards the surface (Watanabe et al., 2002; Hurwitz et al., 2009; Pinel and Jaupart, 2005; Pinel et al., 2010). At first order, we choose not to take into account other causes of deformation related to pre-existing heterogeneities, faults and deep plutonic bodies (Michon et al., 2015; Gailler et al., 2018), chemical reactions and hydrothermal alteration (e.g. Barde-Cabusson et al., 2012; Boudoire et al., 2017; Dumont et al., 2019). However our results will drive us to discuss these factors, since they are all interlinked within the multi-scale dynamics of any volcanic system.

After a summary of the state of knowledge at Piton de la Fournaise, Section 3 below presents our numerical approach, the FEM method Adeli, which has been applied to a variety of geodynamic contexts

for years (Hassani et al., 1997; Gerbault et al., 2018). In preamble we present a newly implemented tensile failure criterion and illustrate its potential influence on our specific volcanic setting. First tests display stresses and deformation resulting from a magmatic reservoir of comparable depth and size to that inferred below Piton de la Fournaise, considering separately, the influence of the inflation source's geometry, the bedrocks' strength, gravity alone or topography alone; these results illustrate the relative influence of each factor. In section 4 we illustrate how stress and deformation patterns are affected by the equilibration of topography considering elastic and then elasto-plastic behavior. In section 5 we look at the influence of a magma inflation, either offset below the eastern flank of the volcano simulating a distal dike injection, or centered below the summit at ca. 2.5 km depth simulating the magma reservoir. Finally we compare the resulting deformation patterns with observations and previous works, commenting on the volcano dynamics.

2. Piton de la Fournaise, a summary of the state of knowledge

Piton de la Fournaise is the latest active volcanic manifestation along the track of La Réunion hotspot. It is a 0.5 Myrs old (McDougall, 1971; Gillot and Nativel, 1989), shield volcano culminating at 2632 meters and built on the eastern side of the older Piton des Neiges volcanic edifice (5 Myr old; Gillot et al., 1994). Its surface morphology is marked by the presence of three nested rims, the calderas of Rivière des Remparts, Plaine des Sables, and the youngest Enclos Fouqué with a fully developed horse-shoe shape opened to the East on the Indian Ocean (Fig. **1**).

Ninety-five percent of the eruptions of the last three centuries occurred within the Enclos Fouqué (Chevrel et al., 2021), which also hosts a 400 m-high, 3-4 km-wide central cone. The April 2007 Dolomieu caldera collapse was coeval to the largest historical eruption at Piton de la Fournaise (e.g. Michon et al., 2009). According to Michon et al. (2015), previous volcanic centers concentrate within 4 other main domains besides the Enclos Fouqué. Two domains were active from 60-30 ka, the southern volcanic zone (SVZ), and the NW-SE rift zone linking the N120 axis linking the Piton des Neiges and Piton de la Fournaise summits. This NW-SE, N120 oriented rift zone (the "Plaine des Cafres" area) stands as a main tectonic feature still hosting eruptive vents, and is believed to be an inherited structure (a fracture zone) cutting through the whole oceanic crust (Chevallier and Bachèlery, 1981; Michon et al., 2015). Cross-analysis of geophysical data, geochemistry and volcanic cone morphometry shows that volcanism at the Plaine des Cafres originates from the deep magmatic plumbing system of Piton de la Fournaise (Boudoire et al., 2017).

Eruptive fissures cover the entire volcanic area, and many concentrate in two NE-SE-oriented fracture zones branching on the central cone, forming the typical "Rift Zones" identified in many volcanic complexes (e.g. Canaries, Hawaii, Etna, Michon et al., 2015): these are believed to develop in relation to the mechanical disequilibrium between the "mobile" side of the edifice, open to the ocean (the eastern flank here) and the "locked" side shouldering on the island's interior (to the west). This disequilibrium is maintained by

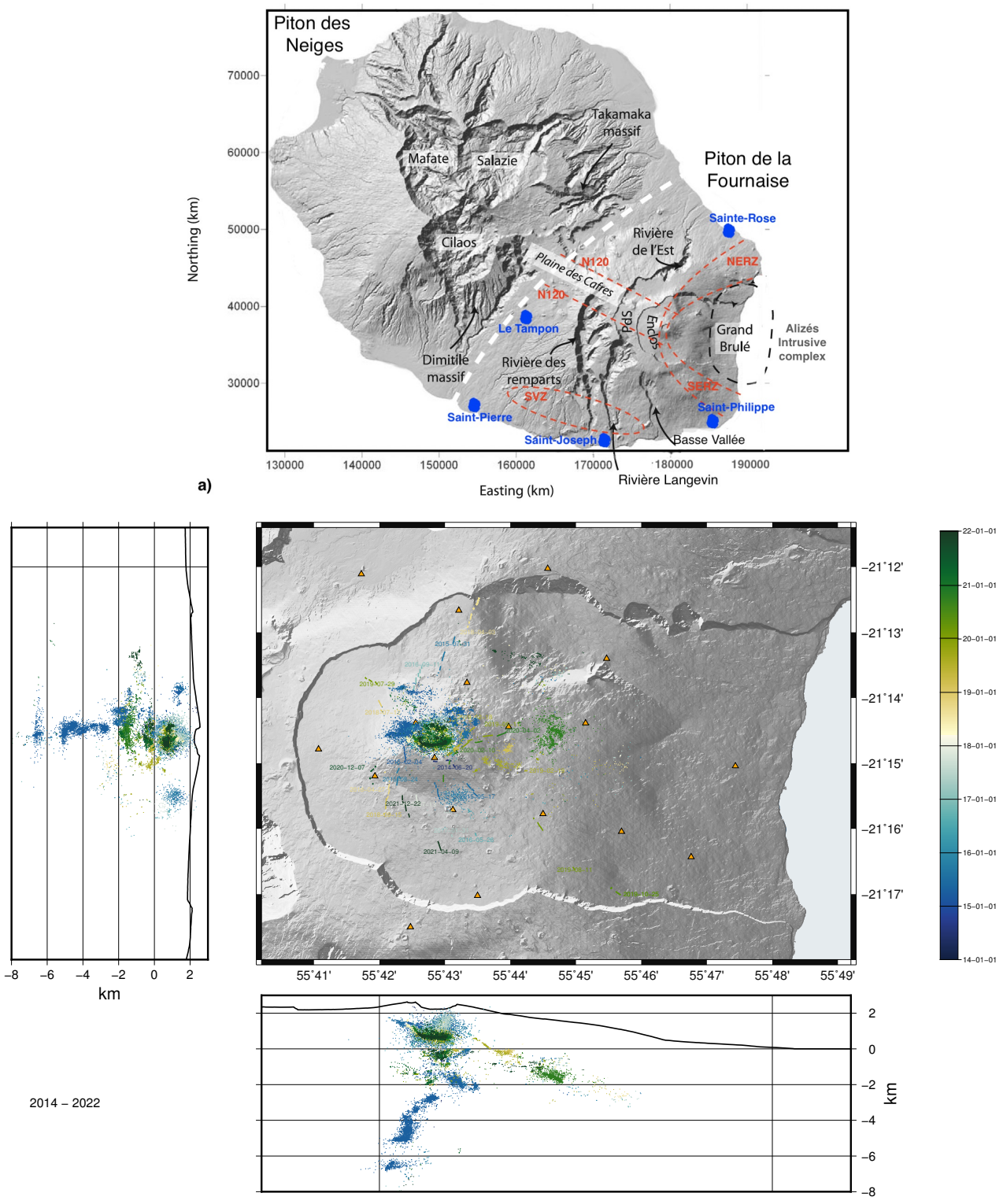

Figure 1: The Piton de la Fournaise volcano occupies the Southern part of Réunion Island: a) Rift zones (NERZ, SERZ and N120) and specific locations names (towns in blue). PdS: Plaine de Sables; SVZ: Southern Volcanic Zone. b) topography of the Enclos Fouqué and earthquake locations between February 2014 and June 2021 in plane view and along north-south and east-west profiles (OVPF, Lengliné et al., 2016; Duputel et al., 2019). FOAG GPNG and FJAG are GPSG stations (triangles).

repeated magma injections and eruptions, with the eastern side of Piton de la Fournaise undergoing a continuous eastward displacement of a few cm/yr (Bachèlery, 1981; Brenguier et al., 2012; Peltier et al., 2015), transiently rising up during major crises, up to 1.4 m in 2007 (e.g. Froger et al., 2015). Volcanic eruptions along these NE (ca. N25) and SE (ca. N155) Rift Zones and outside the Enclos Fouqué, are reported to have been mostly active from ca. 5 ka to 2.8 ka (Michon et al., 2015, and references therein). With rare eruptions outside the Enclos Fouqué, a spatial alternation is observed in eruptions locations between the SE and the NE rift zones inside the Enclos Fouqué, especially since 2007 (Dumont et al., 2022). Michon et al. (2015) proposed a switching mechanism of the tensile stresses orientation between these rift zones and the eastward motion of the volcano's eastern flank, coeval with magma propagation at depth from vertical -dike- injections to shallower -sill- intrusions.

Furthermore, the fissures and fractures network in the vincinity of the central cone were categorized into 3 main groups by Michon et al. (2009): ca. N20 and ca. N65 oriented eruptive fissures opened perpendicular to the slope, concentric fractures parallel to the Bory and Domolieu crater scarps, and linear flank structures cross-cutting several geological units (Fig. D.1). It is debated whether some of these deformation zones are R' shear structures associated with the eastern flank slump motion or instead, structural features associated with the vertical plug exerted by magma intrusion (Carter et al., 2007; Michon et al., 2009).

The magma that feeds present-day eruptions originates from an aseismic, partially molten horizon centered below the central cone, at a depth of about 2 km below the summit (Peltier et al., 2009; Di Muro et al., 2014; Lengliné et al., 2016). This horizon is referred to as the *shallow* magma reservoir. Dikes are identified to rise from this horizon and propagate towards the surface. At greater depth, seismicity initiates from a ca. 20-30 km depth in a N20 oriented domain set in between the Piton des Neiges and Piton de la Fournaise, then rises up from 20 to 10 km depth generally along the N120 NW-SE rift zone, to focus nearly below the central cone at ca. 10 km depth (Michon et al., 2015; Duputel et al., 2021). Between 1998 and 2007, surface displacements occurred by cycles, after many summit-proximal eruptions during which the E-W component of the horizontal stress would increase (Peltier et al., 2008; Got et al., 2013). This was understood as a process of stick-slip elasto-plastic displacement of the eastern flank in response to pressurization of the shallow magma reservoir that led to major distal eruptions (Got et al., 2013). Densification of the seismometers network from 2013 allowed to improve seismicity location. While earthquake location techniques are strongly dependent on the choice of a velocity model (Lomax et al., 2000), the persistent seismicity that occurs offset with respect to the central cone is currently shown to display an inclined trend eastward 2 km below sea level (*bsl*) below the eastern flank, with slightly shallower south and northern edges. Hence its "cup" shaped designation. Enhanced during magma injection events, it also persists in between them (Figs. 1b, D.2, Duputel et al., 2021).

The goal of the present study is to analyze how the observed persistent seismicity pattern may be linked to the typical topography of Piton de la Fournaise and to dike injection or inflation of the shallow magma

reservoir. We will not incorporate the effect of deeper magma reservoirs at ca. 8 km and 20 km depth *bsl* (Prôno et al., 2009; Di Muro et al., 2014; Lengliné et al., 2016), nor will we test the role of pre-existing weak faults or intrusion zones such as did Michon et al. (2009) and Chaput et al. (2014). Although these studies will be mentioned again when discussing our results, here instead, we ask whether it is possible to *form* a deformation zone similar to the recorded seismic cup pattern *above* ca. -4 km depth, in relation to its steep asymmetric topography and standard magma injection events. Is there a peculiar state of stress associated with gravitational loading, or is it necessary to invoke pre-existing heterogeneity zones? Is the persistent seismic "cup" pattern a rather passive feature or instead a potentially active destabilizing, large-scale shear zone ? Is it activated with the complementary load exerted by repeated magma reservoir inflation or instead by dike injections ?

3. Numerical method, model setup and preliminary tests

3.1. ADELI: a standard FEM for elasto-plastic modelling

Adeli is a Finite Element method (FEM) that resolves the quasi-static equation of motion by using the numerical relaxation method (Cundall, 1988). This time-explicit method was shown to handle well the initiation and propagation of brittle elasto-plastic shear zones throughout the crust (Poliakov et al., 1993; Gerbault et al., 1998). Adeli has been used for decades to model various elasto-visco-plastic rheologies in geodynamics and volcanology (Hassani et al., 1997; Chéry et al., 2001; Got et al., 2008; Cerpa et al., 2015; Gerbault et al., 2018). Details on the numerical method can be found in these publications and in Appendix A, and a repository link is provided in the *Code and Data Availability* section.

3.2. Combining shear and tensile failure for an elasto-plastic rheology

Here, we use non-associated Drucker-Prager elasto-plasticity combined with a tensile failure criterion. Tensile failure was not accounted for in Adeli until 2019, and is now implemented based on the approach described in Itasca Flac's manual; details are provided in Appendix A. While the Drucker-Prager criterion depends on the material cohesion C and friction angle φ, tensile failure is assumed to depend on a critical mean pressure threshold p_t. Assuming constants $\alpha = \frac{6\sin\varphi}{3-\sin\varphi}$, $p_0 = \frac{C}{\tan\varphi}$, the domain of admissible stresses is delimited by a truncated cone in the stress space (Fig. **2**), defined by the Drucker-Prager yield envelope (f_s) and the tensile yield envelope (f_t), assuming $p_t \leq p_0$ (we use further $T = p_t$ for conveniency):

$$\begin{cases} f_s(\boldsymbol{\sigma}) = J(\boldsymbol{\sigma}) + \alpha(p - p_0), \\ f_t(\boldsymbol{\sigma}) = p - p_t, \end{cases} \tag{1}$$

where $p = \mathrm{tr}(\boldsymbol{\sigma})/3$ is the mean pressure and $J_2(\boldsymbol{\sigma}) = \sqrt{3/2}\|\boldsymbol{s}\|$ is the second invariant of the deviatoric stress $\boldsymbol{s} = \boldsymbol{\sigma} - p\boldsymbol{I}$. Strain invariants are defined similarly with respect to the strain tensor $\boldsymbol{\varepsilon}$ and will be displayed for the models below (cf. **Appendix A**):

- the total shear strain $J_2(\boldsymbol{\varepsilon}) = \int_0^t \sqrt{\frac{2}{3}} \|\dot{\boldsymbol{\varepsilon}}\| \mathrm{d}t$, and the effective plastic shear strain $\varepsilon_p(t) = \int_0^t \sqrt{\frac{2}{3}} \|\dot{\boldsymbol{\varepsilon}}_p\| \mathrm{d}t$,
- the mean strain is the tensor's trace $I_1(\boldsymbol{\varepsilon}) = \mathrm{tr}(\boldsymbol{\varepsilon})$, which displays dilatational zones when positive,
- the shear strain component ε_{zx}, acts along the vertical direction z (negative downwards, origin at sea level), and the eastward direction x,
- differential values are sometimes plotted, subtracted from values prior to magmatic pressurization.

Note that the convention here is that compressive stress is negative. A Table summarizing the meaning of parameters and symbols can be found in **Appendix A**. Two benchmarks are presented in **Appendix B** to validate the implementation of tensile failure: uniaxial traction and compression of a pierced plate. Whereas the first case displays analytical solutions the second one does not, and we welcome the community to share benchmarks for such implementation.

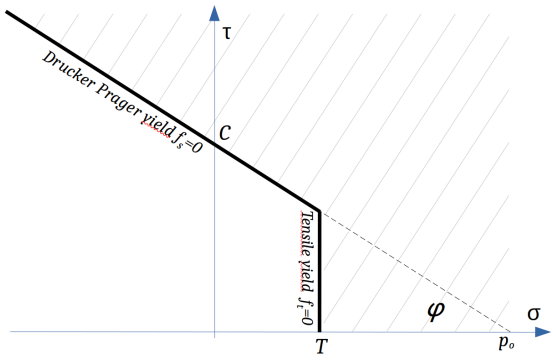

Figure 2: Combined shear and tensile yield envelopes in the first and second stress invariants space (σ, τ) (modified from Itasca FLAC user manual, parameters from eq. 1). $T = p_t$ is the tensile strength, $C = p_0/\tan(\varphi)$ the cohesion, and φ the friction angle. The shaded domain delimits the prohibited stress field (elastic behavior occurs below the yield envelopes).

3.3. Shear and tensile failure around an inflating cavity, no topography

We start our modelling approach with a standard configuration used to model magma reservoir inflation below a flat surface (e.g. Sartoris et al., 1990; Trasatti et al., 2003; Bonaccorso et al., 2005; Currenti and Williams, 2014; Gerbault et al., 2018). Our three-dimensional (3D) setting is similar to that adopted by Gerbault et al. (2018) for an elasto-plastic medium, with the addition of a tensile failure criterion as described above. The inflating source is defined as an ellipsoid cavity of geometry similar to that inferred for the shallow reservoir below Piton de la Fournaise (cf. section 2): its center is located at $z = -2$ km (vertical axis negative downward), its Y and Z semi-axis are equal to 0.5 km, and its X semi-axis is equal to 0.75 km, hence elongated in the East-West orientation later on. The lateral borders are set free-slip whereas the top surface is set stress free. A step-wise increasing pressure is applied at the reservoir's walls so that stresses and deformation then propagate progressively throughout the domain. On the appropriateness of applying an overpressure rather than a displacement, the reader can refer to (e.g. Sartoris et al., 1990). Note also

that only a quarter of the model domain is considered because of radial symmetry, saving computational cost: the modeled domain is a cube of edge length 50 km and mesh resolution reaches 75 m at the cavity walls.

Model name	Fig.	Source axes/depth (km)	Tensile and shear strengths	Gravity	Topo	Surface Disps (m)
M1	3	I2: 0.75-0.5-0.5 / -2	$T, C = 1, 5$ MPa, $\varphi = 3°$	OFF	0	Ux=0.027 Uz= 0.083
M2	3	I2: 0.75-0.5-0.5 / -2	$T, C = 1, 5$ MPa, $\varphi = 3°$	ON	0	Ux=0.022 Uz= 0.068
M3	3	I3: 1.5-0.5-0.5 / -2	$T, C = 1, 5$ MPa, $\varphi = 3°$	OFF	0	Ux=0.045 Uz= 0.170
M4	3	I3: 1.5-0.5-0.5 / -2	$T, C = 1, 5$ MPa, $\varphi = 3°$	ON	0	Ux=0.040 Uz= 0.142
M5	4	I1: 0.06-0.5-0.5 / -1	$T, C = 3, 5$ MPa, $\varphi = 3°$	OFF	PdF	Ux=0.043 Uz= 0.090
M6	4	I1: 0.06-0.5-0.5 / -1	$T, C = 3, 5$ MPa, $\varphi = 15°$	OFF	PdF	Ux=0.032 Uz= 0.060
M7	4	I2: 0.75-0.5-0.5 / 0.	$T, C = 3, 5$ MPa, $\varphi = 3°$	OFF	PdF	Ux=0.039 Uz=0.072
M8	4	I2: 0.75-0.5-0.5 / 0.	$T, C = 3, 5$ MPa, $\varphi = 15°$	OFF	PdF	Ux=0.022 Uz=0.045

Table 1: Models testing independently the influence of gravity, topography, strength and source geometry. First four cases with a flat surface test gravity and the inflating source geometry (semi-axis a_X varies for I1,I2,I3). I2 geometry is similar to that of the reservoir below Piton de la Fournaise ('PdF'). Next four cases illustrate the influence of PdF topography without gravity, for distinct source geometries and bedrock strength (tensile strength T, cohesion C and friction angle φ). Young's modulus in all cases is 10 GPa. The maximum surface displacements (last column) are for an overpressure $DP = 10$ MPa.

Since the influences of inflating source geometry and gravity on elasto-plastic deformation were discussed in the studies cited above, here we only recall key results in the framework of Piton de la Fournaise. The influence of the source's elongation is readily explained with the increasing vertical stretching at its tips upon inflation at the walls, which facilitates tensile failure there. The influence of gravity in turn, appears in the normal stress acting on potential failure planes : the deeper the overpressure source, the more negative the mean stress, away from the tensile threshold. But if the rock mass is considered undrained, then fluid overpressure cancels out the normal component of the stress field. This key role of interstitial fluids was first expressed by Terzaghi (1943) and King Hubbert and Rubey (1959), with pore pressure (p_f) written proportional to the overburden weight ($\rho.g.z$ at depth z). Hence, observations of hydrostatic and sometimes lithostatic fluid pressures in deep wells worldwide have led to the understanding that rocks strength can be reduced in the first couple of kilometers depth (e.g. Suppe, 2014). One can then either assume that gravity cancels out or that the "effective" friction is low. The frictional yield can then be expressed with the effective friction (φ) instead of the intrinsic friction (ϕ), so that $\tan\phi \cdot (\sigma_n - p_f) \sim \tan\varphi \cdot \sigma_n$. Recall that this influence of fluid overpressure on effective strength was also the argument used by Iverson (1995) and Reid (2004) to increase the depth at which rock wedges may destabilize (hydrothermal fluid overpressure would propagate from magmatic sources).

To assess these effects, here we display a first series of four models, with two inflating source geometries and with gravity turned "on" or "off". The bedrock has an elasto-plastic rheology with parameters $E = 10$ GPa, $T = 1$ MPa, $C = 5$ MPa and friction angle $\varphi = 3°$ (Models M1 to M4, Table 1). Figure **3** summarizes

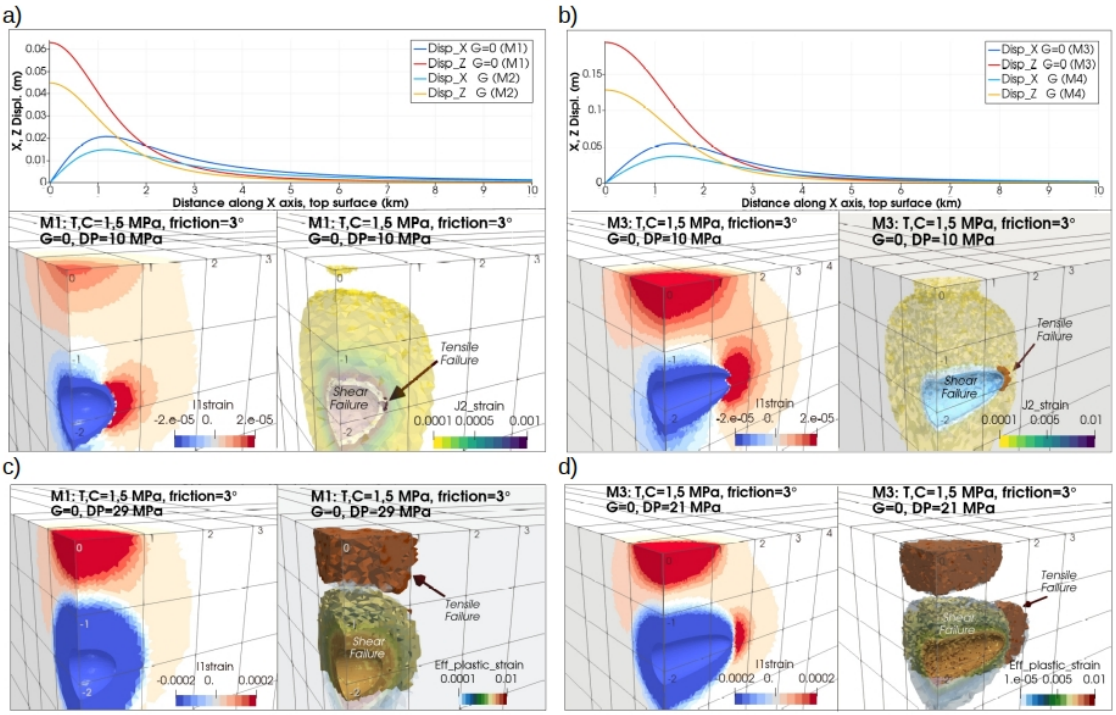

Figure 3: Inflation of a magma cavity below a flat surface in elasto-plastic bedrock, for an overpressure $DP = 10$ MPa: **a)** for an elliptical magma source with semi-axes $a_Z = a_Y = 0.5$ km, $a_X = 0.75$ km (model M1). **b)** for an elongated source with horizontal axis $a_X = 2$ km (model M3). Figures display 3D views of the total shear strain and the effective plastic strain (top-left) and the mean strain (bottom-left, red for dilatation and blue for constriction). Note that tensile failure only occurs at the tip of the elongated source (b). To the right, vertical (z) and horizontal (x) displacements at the surface, with the additional cases with gravity "turned on" (M2 in a, and M4 in b), and x and z displacements on a vertical section along plane Y=0. **c-d)** Same models once overpressure exceeds 29 MPa for M1(c) and 21 MPa for M3(d): the mean stress to the left, and domains undergoing shear (yellow) or tensile (brown) failure modes to the right. Parameters given in Table 1.

the results for an overpressure $DP = 10$ MPa :

- The deviatoric stress decreases at a cubic rate with distance ($1/r^3$, r the distance from the source, Timoshenko and Goodier, 1951) so that failure only initiates in the immediate vicinity of the source even at low strength Figs. 3a,b).

- The surface displacements with the elongated reservoir are almost twice those obtained with the more spherical reservoir (models M1, M2 vs. M3, M4, Figs. 3).

- When gravity is accounted for, the deviatoric stress field needs to overcome a factor of the overburden weight ($\rho.g.z$) for failure to occur, hence no failure occurs at DP=10 MPa. Hence models with gravity "on" display similar patterns to models without gravity, and there is no point in displaying them. Only the surface displacements are ~ 15 % lower than without gravity (due to lack of plastic behavior).

- "Without" gravity, the elongated reservoir develops greater tensile stresses at its long axis tip, because the exerted pressure on the walls tends to stretch them vertically. Tensile failure initiates there (Fig. 3b). The mixed tensile and shear failure mode that appears at the sharp intersection corner between the two yield envelopes (**Appendix A**), is not captured here because of both too low mesh resolution and low temporal sampling frequency.

- Brittle failure expands throughout the crustal domain: in M1 tensile failure barely initiates at the very tip of the longest lateral edge (red zone in Fig. 3a). With increasing overpressure it mainly develops at the surface above 1 km depth, while shear failure dominates around the reservoir (yellow zones in Fig. 3c). In contrast in M3, tensile failure initiates and propagates from the tips as a ring-shaped front, replaced by shear failure with increasing overpressure (Figs. 3b, d). Failure domains at the source's edge and near the surface eventually connect with increasing pressure (cf. Gerbault et al., 2012), but only once DP exceeds 21 and 29 MPa for geometries I3 and I2, respectively.

3.4. Building a numerical model for Piton de la Fournaise

We present now models that account for the relief at Piton de la Fournaise. Therefore, the mesh is built using the *GMSH* software (Geuzaine and Remacle, 2009), for a model domain 42 km wide in both X and Y directions, pointing eastward (X) and northward (Y) respectively. The vertical Z direction originates at sea level and points negative downwards. Thickness is constrained by the depth to the Moho, which varies between 14.5 km in the eastern border of the model domain to a maximum of 17.5 km in its south-western corner (Gailler et al., 2018). Surface topography is implemented at the top surface so that the volcano summit stands at coordinate $Xo = 20$ km, $Yo = 25.8$ km. As in the previous models, lateral borders are set free-slip while the top surface is set stress free.

The base of the model is set motionless, a boundary condition that might be questioned: fixing the Moho's base corresponds to assuming that the mantle underneath is infinitely rigid and compensates the surface topography. Actually some magmatic fluids from the mantle below might locally release the rocks strength and impose instead viscous behavior over a certain breadth. Past tomographic studies including P or S velocity models or both (Driad, 1997; Hirn et al., 1999; Gallart et al., 1999; Fontaine et al., 2015) have mentioned the possible presence of magma at the Moho. This is interesting information because it questions the kinematic status at this boundary; indeed, underplated low viscosity magma in sufficient quantity may allow for lateral motion over a broad wavelength due to the search for isostatic reequilibration along the Moho's slope. The detection of this motion by instruments is hindered by its large wavelength, much larger than the Island's size. Hence in the frame of the present work, we do not consider this factor. Our choices of rheological parameters are justified by the following arguments:

- Young's modulus: at Piton de la Fournaise, several studies assume $E = 5$ GPa (Cayol and Cornet,

1998) in order to fit the observed surface displacements with reasonable overpressure values. This also corresponds with Heap et al. (2019)'s proposition based on a review of volcanic rock properties worldwide. However, greater values were considered by Chaput et al. (2014) (70 GPa) and Got et al. (2013) ($E = 50$ GPa). Got et al. (2013) assumed that such a high Young's modulus represented the intact, linear elastic part of the rock mass deformed at small strain, whereas most of the deformation was explained by larger plastic strain. Other authors such as Traversa et al. (2010) consider instead a Young's modulus of 1 GPa, but they explore the first kilometer where dikes intrude near the surface. Therefore here, we opt for an intermediate value of 10 GPa for the entire crustal domain. More advanced models seeking accurate fit with data should obviously account for a depth dependent E, which should best rely on data-based correlations between seismic velocity and density (e.g. Brocher, 2005).

- Shear and tensile strength: these parameters are poorly constrained. For a wide range of rock types, i.e., altered vs. intact domains, hydrated vs. dry domains, superficial vs. crustal scale domains, tensile strength T generally varies between 1 and 5 MPa, cohesion C between 1 and 20 MPa, and friction between 0° and 40°, with low values corresponding to an *effective* value that accounts for pore fluid pressure (Cocco and Rice, 2002; Suppe, 2014; Villeneuve et al., 2018; Heap et al., 2020), see also discussion in Ginouves et al. (2021). While tension and cohesion control the stress thresholds over the first km below the top surface, friction becomes the main control parameter at greater depths. Saffer and Marone (2003) and Collettini et al. (2019) reviewed how fault zones display fluid-assisted reactions at the grain-scale as a general weakening mechanism in a variety of contexts, which lead to interconnected phyllosilicate-rich fault zones and can result in *effective* frictions as low as $\mu = \tan(\varphi) = 0.1$ ($\varphi \sim 7°$). Recall also that a reduced effective friction was invoked to result from the propagation of overpressurized fluids throughout the rock mass below sloped wedges (Iverson and Reid, 1992); similarly here we will see that friction directly shapes the extent of plastic yielding throughout the volcanic edifice. Instead of displaying a cumbersome catalog of tests, we selected here three typical *effective* friction angles to test, $\varphi = 3 - 5 - 10°$.

3.5. Stress and deformation with topography and no gravity

In seeking the role of topography, we first illustrate how the Piton de la Fournaise edifice impacts on the stress and strain fields induced by a magmatic inflation, without gravity. Gravity is added next.

Four cases displayed Fig. **4** illustrate the influence of the inflating source geometry (I1 vs. I2, models M5-6 vs. M7-8), and that of bedrock friction (models M5-7 vs. M6-8, Table **1**). I1 cases describe a narrow vertical intrusion referring to a dike located 1 km east from the crater's center, extending upwards over 1 km (geometry I1). Below, we will use indifferently the term "intrusion" or "injection" to describe the application of an overpressure at the walls of this modeled "dike", regardless of whether magma reaches the surface or

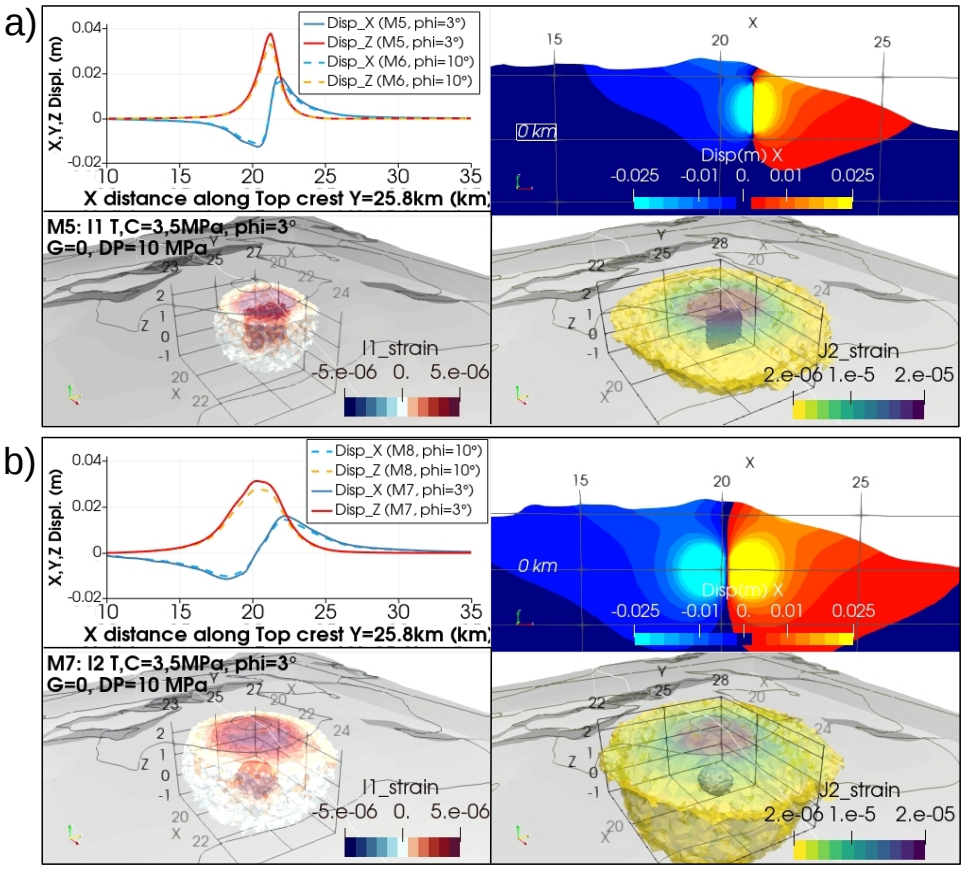

Figure 4: Inflation of a magma cavity with Piton de la Fournaise's topography and *no* gravity (models M5 to M8), overpressure. Displacements (x, z) at the surface (top-right) and along a vertical profile oriented East-West((X direction, top-left). Bottom-left: the mean strain (dilatation in red), and bottom-right, the total shear strain isocontours. An overpressure $DP = 10$ MPa is applied from a narrow dike (I1, **a**) or from an ellipsoidal reservoir (I2, **b**). Contour plots are presented for low friction models (M5, M7) while the surface displacements also display the *higher friction* cases (M6, M8). Parameters in Table 1.

not.As for I2 cases, they describe a magma reservoir located below the submit at center coordinate depth $z = 0.5$ km and of ellipsoidal shape with semi-axes $a_Z = 0.5$ km, $a_Y = 0.5$ km, $a_X = 0.75$ km (references in section 2, and Staudacher et al. (2009)). The results are summarized as follows for an applied overpressure $DP = 10$ MPa:

- With this overpressure, plasticity only initiates in the vicinity of the magma reservoir walls, in both geometries I1 and I2 and for the lowest friction cases (M5 and M7). . Greater friction cases remain elastic (M6 and M8).

- Because of this limited plasticity around the pressure source, displacements are not significantly impacted, barely 1 mm greater for low friction cases (M5 and M7) with respect to the more resistant cases (M6 and M8).

- Both inflation source geometries display similar displacement magnitudes but their extent varies: they extend over about 10 km for the dike (I1) and over almost 20 km for the reservoir (I2) (compare profiles Fig. 4a vs. 4b, top right). Stress and strain deformation isocontours are radial around the inflation sources, little impacted by the asymmetric topography at this scale.

- As of the influence of topography, we compare M7 - Fig. 4b- with M1 - Fig. 3a. We note that i) horizontal displacements have similar amplitudes but they expand along the eastern flank over an additional ca. 5 km with topography, ii) the vertical displacement in turn is reduced by about 2 cm at the summit and it also expands to the east over another ca. 5 km.

- The radial pattern of shear strain follows the circular shape of the Enclos Fouqué caldera (yellowish contours in Fig. 4), for values ranging between $1.5 - 3.10^{-6}$: this depression may thus consistently be interpreted as a mechanical consequence of cumulated micro-shear damage related to repeated magma inflation-deflation cycles (eg. Staudacher et al., 2009; Got et al., 2017).

4. Accounting for gravity: stress and deformation related to topography only

Now, we "turn on" gravity to test the influences on stress and strain patterns, first of the bedrock's strength and second, of the geometry of the inflating source (cases I1 and I2 described in section 3). But a first pre-inflation stage has to be carried out without an inflating source so as to assess the edifice's equilibrium. Hence this section exposes the stress and deformation patterns produced when the medium "equilibrates" when topography alone is imposed. We assume at the onset of the runs that the stress field is isotropic, and we describe the results of four models that assume first an elastic, then an elasto-plastic bedrock (cf. Table **2**).

4.1. Topography, gravity, and elasticity

In model M00 assuming topography, gravity, and only elastic behavior, the resulting stress and deformation displayed Fig. **5** are consistent with analytical calculations on the back of an envelope: the weight of a vertical column at the edifice's summit generates $\sigma = \rho.g.\Delta z = 2500.10.2600 \sim 65$ MPa, which induces a maximum shear stress of about half, e.g. $\tau \sim 33$ MPa. From standard 1D Hooke's law, this induces a deformation $\varepsilon = \tau/E$, which over the width $L \sim 10$ km of the edifice leads to a displacement $dl = L\varepsilon \sim 33$ m. The 3D models here allow to understand where these maximum values are located spatially, and they are not located at the same place: the shear stress (equivalent to $J_2(\sigma)$ in Fig.5a) is maximum immediately below the edifice summit ($J_2 \sim 35$ MPa) while horizontal displacement is maximum (~ 29 m) further along the eastern flank near the shore-line.

Model name	Fig.	Plastic strength	Inflation	Surface Disps (m)	Deformation style
$M00$	5,C.1	Elastic E=10 GPa	-	Ux=27m Uz=-12m	diffuse, broad
$M01$	6,C.2	$T, C = 1.5, 3$ MPa, $\varphi = 3°$	-	Ux=300m Uz=-200m	listric
$M02$	6, C.1	$T, C = 3, 5$ MPa, $\varphi = 3°$	-	Ux=15m Uz=-23m	broad > 5km
$M03$	6	$T, C = 3, 5$ MPa, $\varphi = 5°$	-	Ux=10m Uz=-10m	broad$\sim$ 5km
$M04$	6, C.1	$T, C = 3, 5$ MPa, $\varphi = 10°$	-	Ux=2m Uz=-2m	shallow < 0.5 km
$M11$	7,C.3	Elastic E=10 GPa	Dike I1	Ux=0.015m Uz=0.03m	spike, $dz > dx$
$M12$	7,C.3,C.5	$T, C = 3, 5$ MPa, $\varphi = 3°$	Dike I1	Ux=0.02m Uz=0.02m	asymmetric $dz \sim dx$
$M13$	7,9,C.3	$T, C = 3, 5$ MPa, $\varphi = 5°$	Dike I1	Ux=0.02m Uz=0.015m	asymmetric $dz < dx$
$M14$	7,C.3,C.5	$T, C = 3, 5$ MPa, $\varphi = 10°$	Dike I1	Ux=0.015m Uz=0.03m	spike, $dz > dx$
$M21$	8,C.4	Elastic E=10 GPa	Reservoir I2	Ux=0.013m Uz=0.03m	symmetric + uplift
$M22$	8,C.4	$T, C = 3, 5$ MPa, $\varphi = 3°$	Reservoir I2	Ux=0.025m Uz=-0.03m	broad + subsides
$M23$	8,9,C.4,C.5	$T, C = 3, 5$ MPa, $\varphi = 5°$	Reservoir I2	Ux=0.027m Uz=-0.03m	broad + subsides
$M24$	8,9,C.4,C.5	$T, C = 3, 5$ MPa, $\varphi = 10°$	Reservoir I2	Ux=0.013m Uz=0.03m	symmetric + uplift

Table 2: Models accounting for both topography and gravity. The first four M0x models are without source inflation. The next series test variable source geometries (I1 and I2) and bedrock strength: tensile strength T, cohesion C and -effective- friction angle φ. The resulting surface displacements are provided for an overpressure $DP = 10$ MPa. See text for details.

Here, Young's modulus E=10 GPa was assumed. Naturally, multiplying E by 2 leads to displacement magnitudes divided by 2, hence absolute values should be taken with caution, since in the -*real*- Piton de la Fournaise, values of the Young modulus likely vary significantly with depth (cf. Discussion).

Moho depths vary at the base the model domain: values range from 17.5 km depth in the south-western corner to 14.5 km in the north-eastern corner (Gailler et al., 2018). A model with a flat Moho was tested in comparison (not shown here); it produces similar displacement magnitudes but X and Z displacements maxima at the surface are shifted eastward by about 4 km.

This model also illustrates the inherent flaws that appear when one tries to model the mechanical state of such a volcanic edifice; assuming that topography generates an isotropic stress field (eg. Cayol and Cornet, 1998) or that gravity does not control deformation (eg. Gudmundsson, 2006) contrast with our results. Nevertheless, for equilibrium to be maintained over time wih this topography requires additional loading of some sort, e.g. magmatic overpressurization from below, exactly where high stress and strain concentrate. Here we do not state that these models represent the present day stress and deformation fields at Piton de la Fournaise, but we believe that they allow to bracket the potential influence of gravity.

4.2. Topography, gravity, and plasticity

Now we aim at quantifying the influence of a more realistic brittle behavior when Piton de la Fournaise's topography is embedded in the gravity field. To do this, we use the numerical solution obtained above with only elastic behavior as input, and we "turn on" plasticity. Four models allow to test distinct yield strengths (models M01 to M04, Table 2) and to assess to which extent can the edifice domain undergo plastic failure

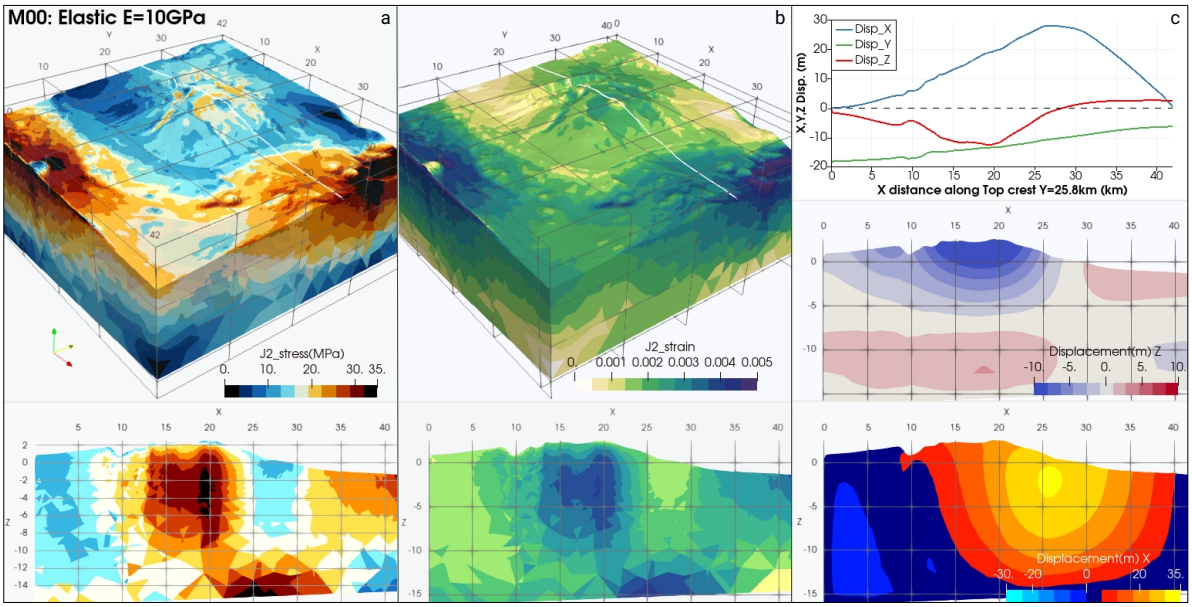

Figure 5: Model M00 considering the topography of Piton de la Fournaise, assuming elasticity in a gravity field. The resulting second invariant of the deviatoric stress, $J_2(\sigma)$, (a) top-3D and bottom-2D views) reaches 35 MPa immediately below the volcano's summit. Shear deformation (b) follows the same pattern with magnitudes ca. 10^{-3}. Displacements (c) display maximum subsidence (z component) at the summit, and horizontal motion in the east-west direction that is maximum near the coastline ($X \sim 26$ km), with 28 m at the surface (top right plots display the x, y, z components along axis $Y = 25.8$ km).

as it 'returns' to equilibrium. The resulting deformation from these models is displayed in Figure **6**, while the resulting stress field is displayed in Appendix Figure **C.1**. Several features are noted:

- In the weakest model (M01, Fig. 6a), the entire edifice fails and forms a clear large scale, listric shear zone encompassing the western edge of the Enclos Fouqué down eastward to the shore line. Shear deformation magnitudes are greater than 0.1, vertical and horizontal displacements achieve several hundreds of meters, and we note uplift to the east below the coastline in $X \sim 31$ km (in red). We are clearly seeing here the general collapse of the edifice.

- Only doubling the value of tensile strength (T) and cohesion (C) impedes this drastic topographic collapse (M02, Fig. 6b). Shear deformation is reduced by an order of magnitude, with displacements of only few tens of meters. Plastic shear failure covers an area of about 10 km around the summit (exceeding the western limit of Enclos Fouqué), reaching about $z = -4$ km depth. It is greatest along a north-west south-east axis passing by the summit and along the coastlines.

- When the friction angle is further increased from 3° to 5° (M03, Fig. 6d), deformation magnitudes and displacements are both reduced by another factor 2, but plasticity still occurs over about 1 km below the summit area.

- In the 'strong' model with friction angle set to 10° (M04, Fig. 6c), plastic deformation is again reduced by an order of magnitude and only affects the upper $\sim$ 500 m below the summit area. Displacements achieve only a couple meters. Despite these huge differences in amplitudes, the displacements in models M02-M04 adopt a similar pattern that extends along the eastern flank of the edifice.

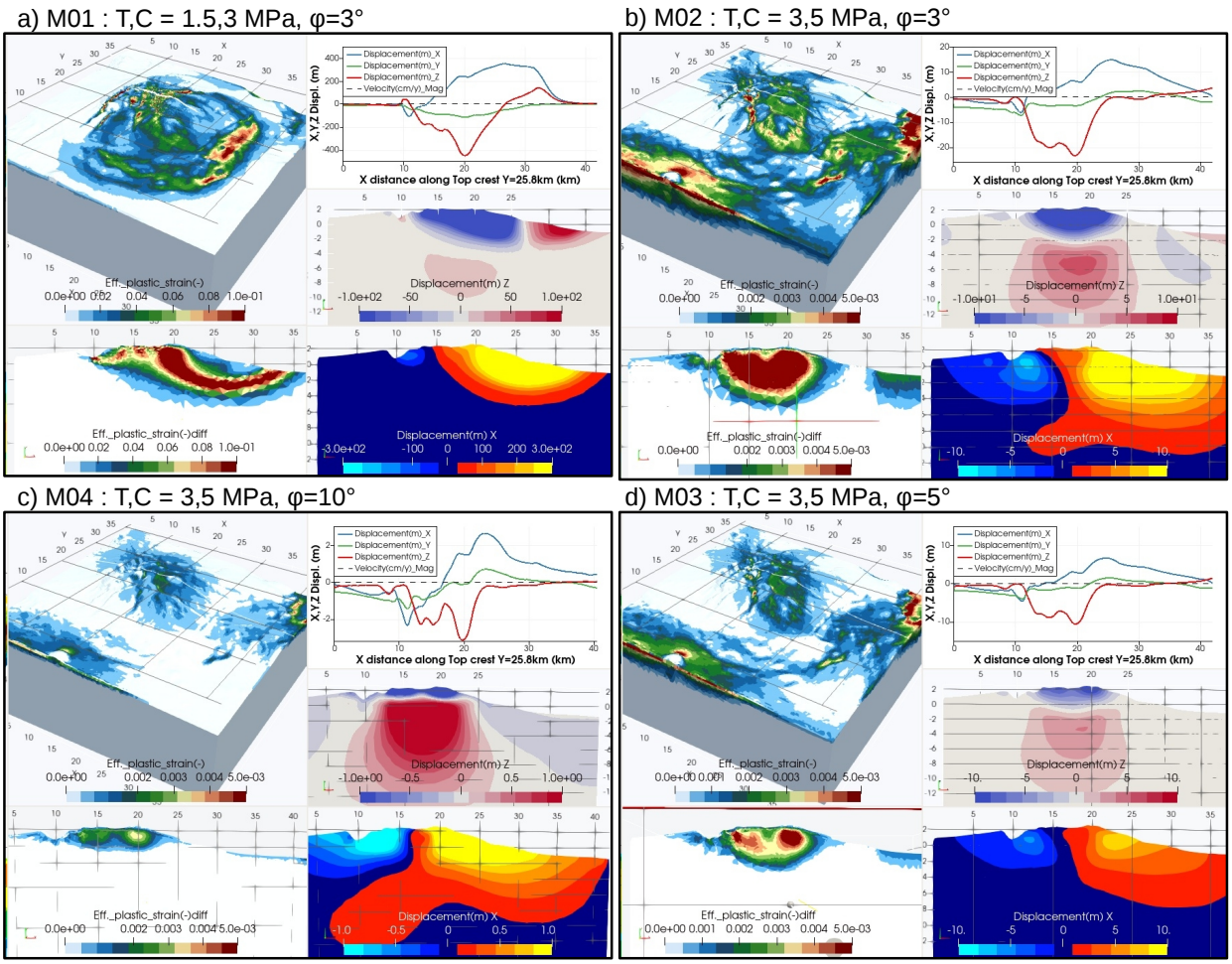

Figure 6: Modeled deformation due to topographic loading only, testing four distinct elasto-plastic strengths. **a)** case M01, with $T = 1.5$ MPa, $C = 3$ MPa, $\varphi = 3°$, **b)** case M02, with $T = 3$ MPa, $C = 5$ MPa, $\varphi = 3°$,**d)** case M03, with $T = 3$ MPa, $C = 5$ MPa, $\varphi = 5°$, **c)** case M04, with $T = 3$ MPa, $C = 5$ MPa, $\varphi = 10°$. Left column : the effective plastic shear strain (ε_p^{dev}) in 3D (top) and in 2D vertical section along Y=25.8 km (bottom). Note two orders of magnitude difference in scale with case (a). Right column : the displacement components (in addition to the elastic solution, Fig. 5). At the surface along axis Y=25.8 km (up-right) and for components z (vertical, middle) and x (east-west, bottom). Note again the different magnitudes.

While it has become customary to relate modeled plastic strain to seismic behavior (e.g. Sibson, 1994; Chéry et al., 2001; De Barros et al., 2019), this requires assuming a relationship between a certain amount of (shear or volumetric) strain to seismicity. However, this assumption remains empirical, very scale-dependent, and to our knowledge there are no critical intensity values that can be assimilated to seismic behavior unequivocally.

Nevertheless, geometrical patterns can be compared. Hence, when asking whether the observed cup shape seismicity observed at Piton de la Fournaise is caused by the yielding of the rock mass in relation to its topography only, we analyze the plasticity pattern obtained in the models above and observe that :

1. obviously the listric shear zone obtained in the weakest model (M01) reminds of the observed seismic cup shape. But this result means that if that was the real state of Piton de la Fournaise, it would not be able to maintain itself at the height at which it stands today. Hence, as this model provides an extreme solution of what would happen if the volcano was to destabilize entirely, it tells us that the general strength of the edifice has to be higher than what is assumed there. Furthermore Appendix Fig. **C.2** shows that this listric trend does not fit the straightness of the persistent seismicity.
2. The other model cases with greater strength produce reduced magnitudes of deformation (by one to two orders), down to depths directly linked with the friction angle. This deformation pattern is rather symmetric around the summit and also trends down slope along a south-east orientation (see Fig. 6b and Fig. 6d in three dimensions). In contrast the observed seismicity cup rather trends plain east. Hence this deformation pattern does not fit the observed persistent seismicity.

For these two reasons, we conclude that topography alone cannot explain the seismicity *cup* observed at Piton de la Fournaise. Therefore next, we simulate magma inflation processes to assess their influence on the overall stress and strain patterns.

5. Influence of magma inflation geometry and bedrock rheology

Now we investigate how magma overpressure affects the "preloaded" stress and deformation patterns (obtained in the previous section). Therefore we consider the two different pressure sources considered in section 3, first the "vertical and narrow" one that represents a vertical dike injected 1 km east from the summit, termed I1, and second, the "wide and deep" ellipsoid source centered at coordinate depth $z = 0.5$ km, that represents the magmatic reservoir. The aim is to identify which one of these two sources produces deformation patterns that could best be linked to the observed seismicity.

5.1. Influence of a narrow vertical, distal intrusion

We model the impact of a narrow vertical inflation below the eastern flank of Piton de la Fournaise, that may be attributed to a dike that feeds distal eruptions in association with eastward motion (e.g. Peltier et al., 2009; Got et al., 2013). Got et al. (2013) showed with 2D numerical models that elasto-plastic behavior can amplify and localize deformation with respect to elastic behavior, then explaining GPS values of several tens of centimeters measured during eruptive crises. Our aim here is not to reproduce nor fit exactly such data, but rather to display in 3D the typical deformation pattern induced by such an injection.

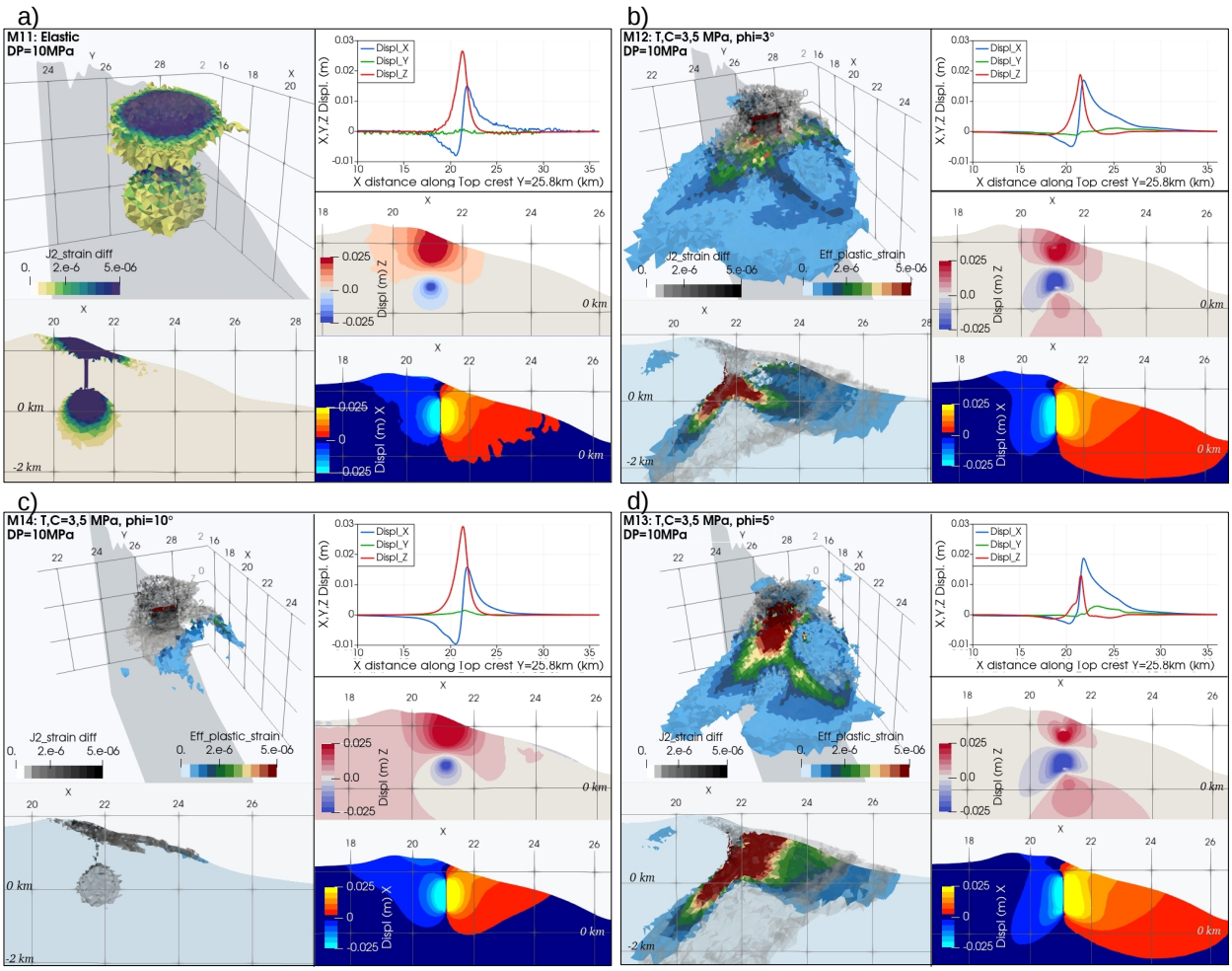

Figure 7: Models of a vertical injection (I1) below the eastern flank of the volcano, with 4 distinct elasto-plastic strengths: **a)** elastic (M11), **b-c-d)** elasto-plastic with tensile threshold $T = 3$ MPa, cohesion $C = 5$ MPa and friction φ equal to 3° (b), 5° (d), 10° (c). For each cases the left column displays 3D and 2D views of the effective plastic strain superimposed on the total shear strain (colored and grey colorbars, respectively). Displacements are shown on the right : top panel for the top surface, middle and bottom panels for components Z and X, respectively. Note the distinct patterns in the weak (b,d) and strong (a,c) cases. Plots display differences with the pre-inflation step.

The injection I1 is designed to initiate below the surface with a base set at depth $z = 0.75$ km. It extends vertically for 1 km and strikes north-south, 1 km east from the volcano's summit (I1 is a meshed parallelepiped). An incremental overpressure (DP) is applied at the walls of this structure, superimposed on the mechanical state obtained in the previous 'pre-inflation' stage. We define four models to test distinct bedrock strength: M11 is elastic, M12 and M13 have a weak bedrock friction ($\varphi = 3°$ and $5°$) and M14 has a stronger bedrock friction ($\varphi = 10°$).

Figure **7** shows that the resulting deformation pattern expands from the inflation source outwards to the surface, mobilizing portions of the eastern flank. It can differ from the previous tests without either

topography or gravity :

- The model with elastic rheology (Fig. 7a, M11) shows that shear strain develops radially around the upper and lower tips of the dike. The free surface above the dike dilates, with vertical uplift (maximum 3 cm) and slightly greater horizontal displacement to the east than to the west because of the asymmetric topography (maximum 1 cm). These patterns resemble the models without gravity, Fig. 4a (M5, M6). Complementary plots are displayed in Appendix Figure **C.3**.

- In models M12 and M13 with a weak bedrock friction (Figs. 7b,d), plastic deformation (effective plastic strain) develops maximum at the base of the dike intrusion near $z = 0$ km depth, and expands sideways forming an inclined "curve" down to $z \sim -1$ km along the edifice's eastern flank, which then rises back up to the surface just above the coastline at $X \sim 26$ km. When looking from above, radial shear zones oriented south-east north-east join back down slope in $X \sim 26$ km, connecting with the shear zone 2 km underneath. Near the summit and above the dike, the bedrock domain cannot develop much additional failure since it already failed in the 'pre-inflation' stage. Dilatation above the dike is narrower than in the elastic case, uplift is diminished but horizontal motion expands along the eastern flank and increases (maximum 2 cm).

- Model M14 with a greater bedrock friction displays an evanescent plastic domain, restricted to the dike's upper tip and the first ca. 100 m depth along the eastern flank. No sub-horizontal structure appears below the eastern flank (Fig. 7c). Surface displacements are similar to the elastic case.

- Displacements differ in both sets of weak and strong models: horizontal displacement is greater and more distributed over the extent of the eastern flank in the low friction models (M12 and M13) in contrast to the resistant models. These results are consistent with the patterns measured at Piton de la Fournaise in association with distal injection events (e.g. Got et al., 2013; Smittarello et al., 2019), noting that magnitudes differ with these studies due to distinct choices of E and DP (cf. test with $E = 50$ GPa displayed in Appendix E.1).

5.2. Influence of a "central-ellipsoid" magma reservoir

Now we aim at quantifying the deformation induced by a deeper and elliptical magma reservoir, as revealed by numerous studies at Piton de la Fournaise over the years (e.g. Peltier et al., 2015). Its shape and location are subject to debate, but the consensus is a center depth around coordinate $z = 0.5$ km and an east-west major axis extending for a bit more than 1 km. This geometry I2 (similar to the one defined in section 3) is included as a meshed ellipsoid in models M21 to M24 (Table 2).

An incremental overpressure applied at the walls of this reservoir produces stress and strain that are displayed in Figure **8** for $DP = 10$ MPa. These patterns resemble those produced by the distal vertical

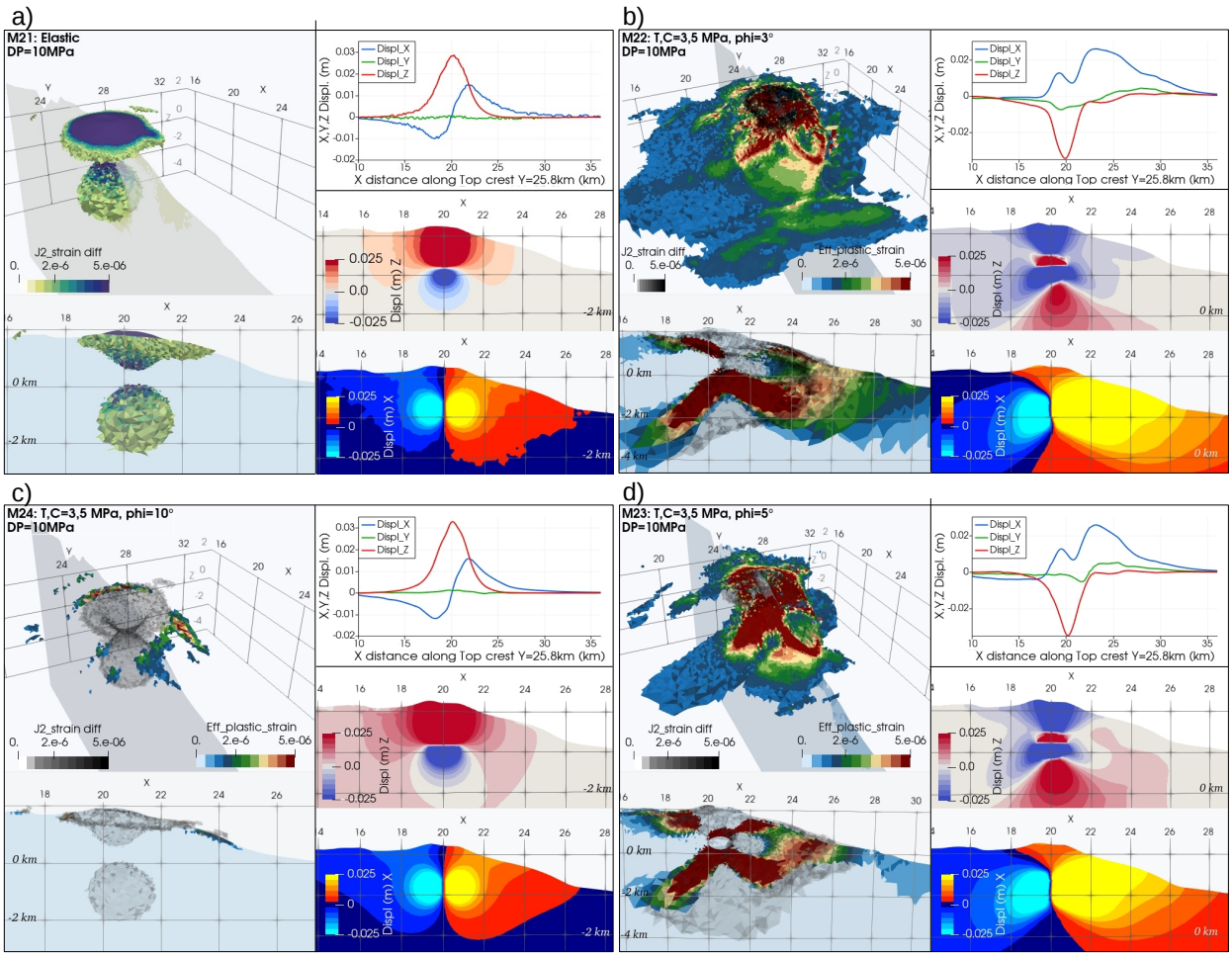

Figure 8: Models with an inflating magma reservoir (I2). Four cases with variable bedrock strength: **a)** elastic ($M21$), **b-c-d)** elasto-plastic with tension and cohesion $T, C = 3, 5$ MPa and friction φ equal to 3° (b), 5° (d) and 10° (c). Left: 3D and 2D views of the effective plastic strain superimposed on the total shear strain (colored (a) and grey (b-c-d) colorbars). Right: the displacements (top are surface curves, middle is vertical Z component, bottom is horizontal X component. Note the distinct patterns in the weak (b,d) and strong (a,c) cases. Plots and displacements are measured from the onset of inflation.

intrusion models : the displacement magnitudes are similar, the plastic strain is asymmetric with isocontours dipping along the eastern flanks of the volcano. As we note that the eastern edge of the modeled magma reservoir (I2) coincides with the deepest portion of the modeled dike intrusion (I1), we identify that this specific area of overpressure source, common to both geometries, controls the observed surface deformation patterns below the eastern flank. Further remarks can be made:

- the total shear strain contours occupy at the surface a similar breadth to that of the circular boundary of the Enclos Fouqué heights (similarly to models without gravity, Fig. 4b). Most of the shear strain is plastic when friction $\varphi \leq 5°$, and it expands along the volcano's east and south-east flanks. An "arm"

of plasticity develops south-east, indicating that this domain might present some structural fragility (top 3D views in left columns of Figures 8a and Appendix **C.4**).

- Here again the maximum depth of the plastic domain depends on the bedrock's frictional strength: it barely affects a few hundred meters depth if the friction angle is 10° or more (model M24), but it reaches $z \sim -2$ km if the friction angle is in the range 3-5° (models M22, M23).

- Figs. 8b,d show that radial "eccentric" shear zones develop at the surface from the edifice's summit down east- and south-wards, forming the typical 3D patterns that have been observed and modeled elsewhere resulting from brittle material being indented from below (Nádai, 1963; Ernst et al., 1995; Holohan et al., 2013; Gerbault et al., 2018). Hence these modeled structures might offer a complementary explanation to the interpretation of radial and oblique eruptive fissures or fault zones reported at Piton de la Fournaise (e.g. Michon et al., 2009, Appendix D.1). This will be further discussed below.

- The domain immediately above and about 2 km around the summit (e.g. the central cone), displays a distinct state of stress depending on bedrock strength; dilatation and uplift occurs when the bedrock is strong (models M21, M24, Figs. 8a,c, C.4), following standard elastic behavior. In contrast, a more complex pattern of alternating levels of dilatation and constriction develops when the bedrock is weak (models M22, M23, Appendix Fig. C.4a,b), and the summital area subsides. This occurs because the bedrock fails plastically there, in between the reservoir's roof and the top surface, leading to coeval uplift and collapse (like an extrado). Note that the models provide an 'integrated' picture of the edifice's response to pressurization. In contrast at Piton de la Fournaise, the central cone records surface uplift -or no significant vertical motion- during reservoir pressurization, and subsidence after eruptions. This discrepancy between modeled deformation with observations indicates that other processes than those modeled here also contribute in sustaining the cone (such as repeated magma input).

- Note also that this summit area forms at depth a cone of deformation isolated from the rest of the edifice; in the case of weak bedrock it is bounded by shear zones branching to the center of the magma reservoir. They emerge to the surface to the west in the Plaine des Cafres and to the east at $X \sim 22.5$ km; comparison with observations is discussed below. Such 'shallow' landslides require a more precise geotechnical study.

- Another point to discuss further concerns the modeled failure modes : Figs. C.4 show that shear failure is again, the dominant mode of failure over the entire plastic domain, except in the near surface few hundred meters to the west of the volcanic edifice, upstream of the Rivière de l'Est to the north and upstream of the Remparts and Langevin river canyons, where tensile failure also occurs (when $\varphi \leq 5°$).

5.3. Relating the modeled deformation field and the observed seismicity below the Eastern flank

In the light of the above models, we superimpose the modeled strain patterns and the observed seismicity pattern, Figure **9**. The differential effective plastic strain and the xz component of the strain tensor are both plotted for models M12 and M22. Clearly, the distal injection model (M12) produces a curved shape shear zone below the eastern flank of Piton de la Fournaise that is shallower than the observed seismicity cup by about 1 km. The magma reservoir inflation model in turn (M22) produces a shear zone whose maximum isocontours coincide well with the seismic cup. We add the following comments:

- Our modeled plastic shear strain along this $z \sim -2$ km depth horizon testifies of a process of localized brittle shear failure, supporting the notion of a localized "fault-zone" drawn by the cup-seismicity below Piton de la Fournaise (cf. events depth located by OVPF as red circles in Fig. **10**). Our representation of the xz strain component indicates a more specific orientation of shearing in these directions, consistent with an eastward down-sliding component of the hanging-wall portion of the edifice's flank.

- The domain embedded by the shear strain "cup" can be considered to deform aseismically, eg. by creep (e.g. Poland et al., 2017; Villeneuve et al., 2018; Got et al., 2019; De Barros et al., 2019). Note that seismicity actually does not necessarily occur in damaged domains but rather at its boundaries with surrounding intact rock mass where there are still cohesive bonds to break; in that sense, the seismic "cup" can draw this contour boundary between intact material at depth and already damaged (e.g. 'broken') material near the surface.

- The observed seismicity cluster at the deepest end at $z \sim -2.5$ km and $x \sim 25$ km (C3 in Fig. 1b) correlates with the area in our models where the shear zone 'rotates' from down-east dipping back up-to-the-east. We note that the strain magnitude significantly reduces in this eastward up-dipping portion, which can be linked with the lack of seismicity observed further to the east. This observed seismic cluster stands "upstream" from the Alizés grabboic body that was identified from MT and gravity studies (Gailler et al., 2018, , Fig. 1a).

- The observed seismicity clusters to the south ($z \sim -1.5$ km and $y \sim 26$, C2) km and to the east ($z \sim -2.5$ km, C3, Fig. 1b) could result from locally altered rock domains or a fault zone. Dumont et al. (2019) measured MT anomalies above these seismic clusters (investigation depth 1 km) which would coincide with a N65 fault lineament (Michon et al., 2009). While a pre-existing fault zone is a possibility, our models only indicate that shear strain there may result from the edifice's flank dynamics and not necessarily from a pre-existing fault.

- West from the summit and deeper than $z = -4$ km, the observed seismicity seems to link with the modeled west-down-ward dipping branch of shear strain that results from inflation of the magma

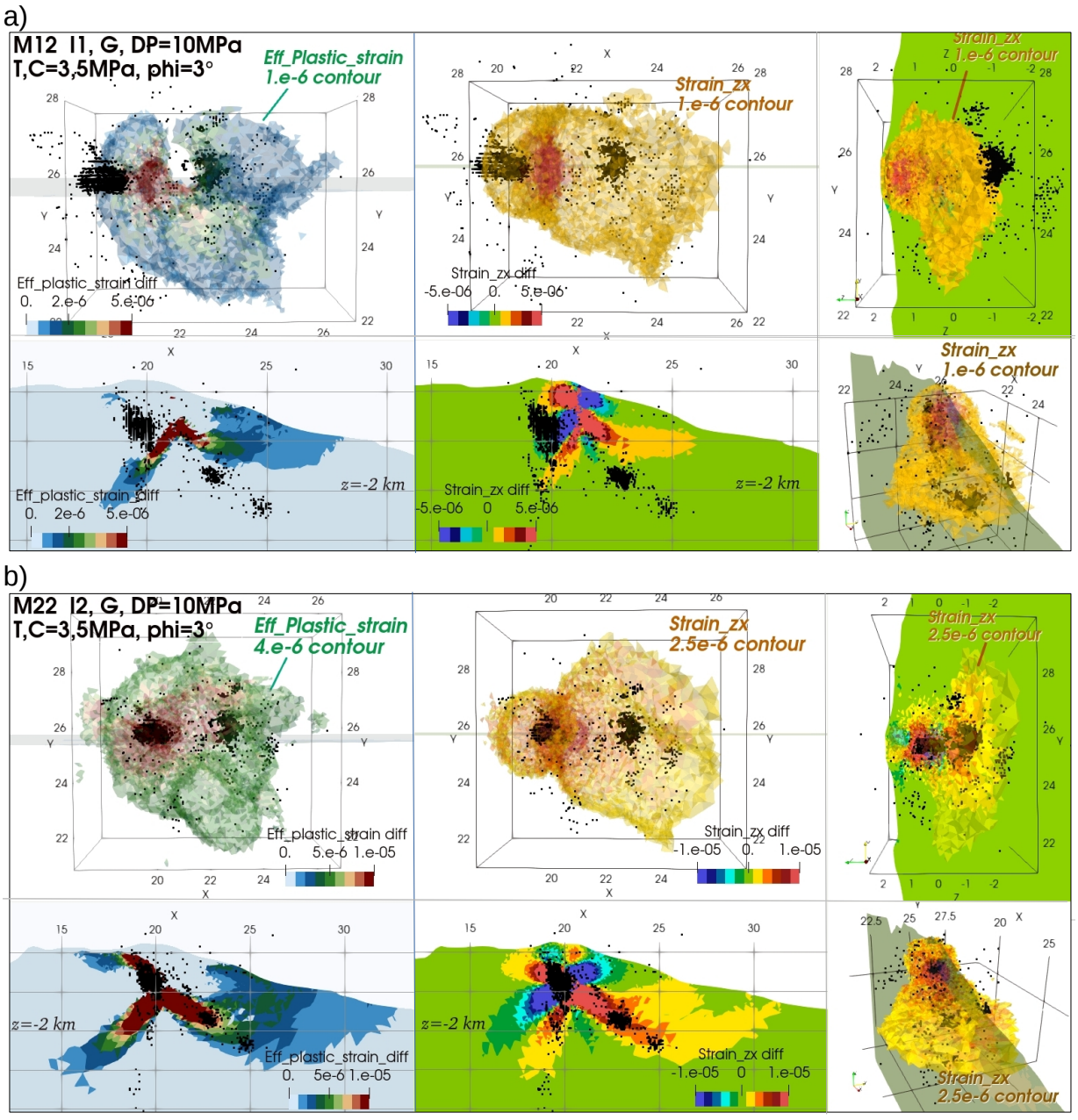

Figure 9: Comparison of the observed seismicity pattern at Piton de la Fournaise (black dots) with the contours of shear deformation obtained numerically in two distinct models. In the column to the right, the effective plastic strain, and to the left, the zx shear strain component. Views are displayed similarly to Fig. 1b, in top view and along profiles in the east-west and north-south direction. **a)** model M12 with a vertical distal injection: high strains remain above ca. z=-1 km depth below the eastern flank. **b)** model M22 with an inflating magma reservoir: the dipping shear zone coincides now better with the observed cup-shape seismicity.

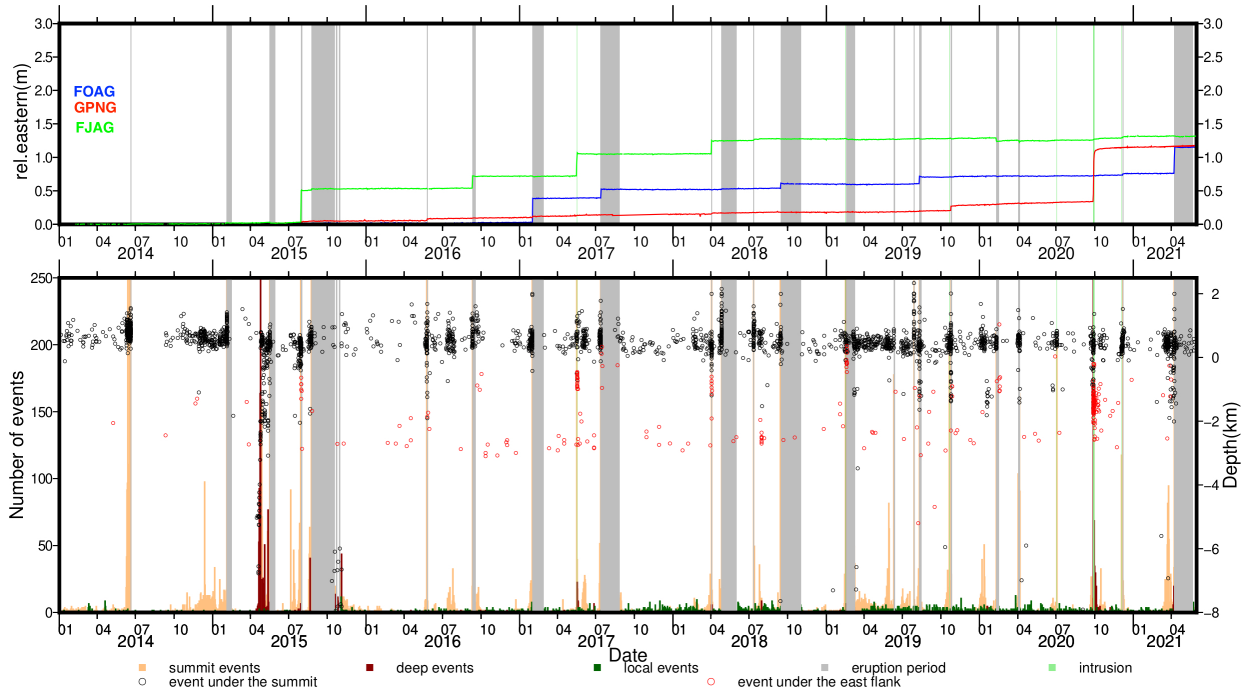

Figure 10: Temporal record of flank motion, seismicity and eruptive activity at Piton de la Fournaise from 2014 to 2021 (OVPF). **a)** Eastern displacements at three GPS stations (FOAG, GPNG, FJAG) located in Fig. 1. **b)** Daily seismicity rate and earthquake depth. Events below the summit are shown with black circles and earthquakes under the east flank are shown in red. Shallow and deep seismicity rates are shown in orange and brown, respectively. Eruptive activity is marked as grey bands.

reservoir. Note that this deformation branch in the models does not develop with high rock strength, which is consistent with the idea that the crust becomes more resistant with depth. However localized weakening by hydro-magmatic fluid flow upon injection may produce seismicity (e.g. White et al., 2011; De Barros et al., 2019), and in fact this deep pattern of nearly vertical seismicity is interpreted as related to magmatic fluids migrating out from the deeper reservoir at ca. $z \sim 8$ km depth (e.g. Battaglia et al., 2005; Michon et al., 2015; Lengliné et al., 2016). We actually note a difference in dip of about 10° between our modeled shear zone and the observed near vertical seismicity trend. Our models simply indicate that either way the dynamic transfer of magma from a reservoir at ca. 8 km depth up to the '0-km-depth' reservoir is kinematically consistent with shear deformation along this trend.

- Our models indicate the development of active conjugate shear zones that form a "cross" centered on the magma reservoir and that accompany its inflation cycles; they witness the 'gravitational' interplay of magma inflation and the inclined eastern flank. These shear zones also developed in previous models (Gerbault et al., 2012, 2018; Holohan et al., 2013, with flat free top surfaces), (Got et al., 2013, or

not). Note then how the three-dimensional structures are organized: while the summit area is uplifting or subsiding depending on the magma reservoir's pulsating inflation cycle, the eastern side forms a material slice that is bordered by eccentric shear zones at the surface and which root at depth: their upper limit links on to the eastern upper branch of the cross-shape shear zone, and their lower limit links on to the east-down-ward dipping cross-shape shear zone down to ca. -2 km depth (e.g. our cup-shape shear zone). The models help us to understand the constrained kinematics associated to this 3D cup-geometry.

- Finally, in our models, the shear zone that we attribute to the observed cup seismicity is also a domain where the trace of the strain tensor switches from dilatational above, to constrictional below (differential values, Figs. C.4a,b). This is a typical feature of tectonic shear zones that delimit locations of stress rotation and display seismicity (e.g. Gerbault et al., 2003; Dorbath et al., 2008). This switch of the mean stress state in turn indicates that magmatic fluids coming from depth within the dilatation zone are impeded to travel further up because they encounter a constricted domain in the overburden (hanging-wall), hence, they remain stuck there. In comparison with the thermal models by e.g. Annen and Sparks (2002), we can say that this state of stress is consistent with magma stacking from below.

6. Discussion

6.1. Numerical assumptions and choice of parameters

A modeling study such as ours can never be exhaustive, and it is clear that accounting for the rheological heterogeneity of the crust at Piton de la Fournaise would allow to better fit a model of the mechanical state with various measured data (seismicity and GPS for instance). But uncertainties increase when having to assume the mechanical properties associated with heterogeneity. Our purpose here was to unveil the influence of first order parameters when considering the gravitational state of a homogeneous edifice, and yet a number of alternative assumptions deserve to be commented.

Whereas a volcanic edifice naturally results from potential energy minimization due to the progressive transfer of deep magmatic material to the Earth's surface (during about 0.5 My in the case of Piton de la Fournaise), our models here were implemented with the sudden influence of topographic load, hence they produce an exaggerated deformation field. However, our comparisons between models accounting for gravity only, topography only, and then combined topography and gravity, show how the latter combination sheds light on the dynamic response of the volcanic edifice to magmatic inflation. Further comparison with other approaches is thus required to decipher real effects from artifacts:

1. We have assumed here a "homogeneous" crustal medium to interpret the seismicity pattern below the edifice's eastern flank, and we have found that the effective rock mass friction has to be rather close to

$3-5^\circ$ than to $\geq 10^\circ$, at least in its upper-most 4 km. While many studies have explored how elasto-plastic properties introduce non-linearity, generating rigid-like block motion bounded by shear zones (Gerbault et al., 1998, 2012), the spatial mechanical heterogeneity of crustal domains also complexifies the deformation signal upon application of a magmatic load (e.g. Trasatti et al., 2005; Gudmundsson, 2006; Masterlark, 2007). At Piton de la Fournaise, both the elastic and plastic properties vary not only with depth but also most probably on inherited kilometric-size domains, identified from i) island-scale geophysical surveys, such as the central cone, the Piton des Sables and the Alizés bodies which were identified down to at least $z = -4$ km depth (e.g. Gailler et al., 2018), and ii) morphological analysis of fissures and rift zones riddling the surface (e.g. Michon et al., 2009). These heterogeneities are expected to exert a first order control on deformation patterns and stress distribution throughout the edifice, with stiffer bodies storing larger deviatoric stress and reducing deformation amplitudes. Moreover, the boundaries of such heterogeneous domains constitute rheologically discontinuous "corners" where seismicity may be enhanced. For instance, the C4 seismicity cluster (Fig. 1b) may testify to a rheological boundary with the more rigid Alizés body. This body may actually block the propagation of the shear zone further to the East, hence act as a buttress that restrains the Eastern flank's motion. The presence of regional fractures or rift zones can also enhance seismicity locally as mentioned by Michon et al. (2015). Now that we understand what are the implications of considering a homogeneous medium, future models will need to confirm whether the observed seismicity actually illuminates "passive" rheological contrasts or instead, potentially "active", threatening large-scale flank motion.

2. In our models, the domain forming the magma source was considered elastic and of Young modulus equal to that of the surrounding bedrock; assigning it other properties can have some impact, and numerical tests -not shown here- show that considering an elasto-plastic intrusion modifies the deformation patterns by about 10%, or that assuming a 10 times more compliant source (as Got et al., 2013) reduces the surface displacements by about a third. The internal thermodynamics can also induce visco-elastic behavior (Novoa et al., 2019). With lack of knowledge of how magmatic sources behave in reality, we can only warn here that the source's rheology also influences model-to-data matching.
3. Here, we have assumed that the dike injection was oriented fully north, following a simple orthogonal prolongation of the 2D model set up by Got et al. (2013). Other injection geometries can be tested, as has been done by previous studies for specific eruptive events (e.g. Fukushima et al., 2005; Michon et al., 2009; Smittarello et al., 2019; **?**). Modifying the geometry of the inflating source in our models would allow comparing our stress and strain patterns with these studies and commenting about distinct loading assumptions. More specifically, the impact of a sill injection below the eastern flank could be further explored (cf. preliminary test in Appendix E.2).
4. Magmas come from the mantle, but we do not know at which rate and in which quantities they migrate from one level to the other. This magma input may occur by discontinuous pulses of small

quantities throughout the porous medium, eg. via porosity type waves (Havlin et al., 2013), or in larger quantities by transient motion that produce anomalies identified by geophysical surveys, at ca. 8 and 20 km depths (Gallart et al., 1999; Fontaine et al., 2015; Gailler et al., 2018). Such magmatic transfer towards the surface is controlled by the regional stress field such as lithospheric flexure (Michon and Saint-Ange, 2008; Gerbault et al., 2017), which should be accounted for in future models.

5. Note that the overpressure that we chose to display, $DP = 10$ MPa, corresponds, for a reservoir of size $Vo \sim 1$ km^3 and a compressibility $\beta = 3(1-2\nu)/E$, to an erupted volume of the order of $dv/Vo = \beta DP \sim 0.0015$ km^3. This value is comparable to estimates of erupted volumes of $0.001-0.013$ km^3 at Piton de la Fournaise, with about half ranging below 0.003 km^3 since 1992 (Roult et al., 2012). Similar magma overpressures of the order of 8 MPa have been proposed for dike injections (Fukushima et al., 2010) as well as for magma reservoir inflation (Peltier et al., 2008). Considering lower values of overpressure in our models actually has small impact that falls within the uncertainty range of other parameters over the scale of the volcanic edifice and crustal thickness. Traversa et al. (2010) proposed changes in magma reservoir overpressure of barely 2-3 MPa at Piton de la Fournaise, based on models of buoyancy driven dike propagation. However they considered a small shear modulus (1 GPa) and low density of the central cone area. This difference in estimated overpressure with ours may be explained with the greater scale and simpler homogeneous medium that we consider here. It may also be reconciled if we consider that the source overpressure does not necessarily depart from an isostatic state of stress, but that instead it departs from a persistently overpressurized source, so that overall the pressure source would achieve ca. 10 MPa above the overburden weight (e.g. as we defined DP here). Next generation models should also consider this point.

6. Additional tests not shown here with friction $\varphi = 7-15°$ develop characteristics closer to the strong cases ($\varphi = 10°$) than to the weak cases ($\varphi = 3, 5°$). This leads us to propose the critical value of $5°$ as effective strength of the volcanic edifice down to about 5 km depth.While this value is close to estimates for Kilauea's decollement zone (Morgan and McGovern, 2005a), the mechanisms at play explaining such low effective friction likely differ, since a specific weak tectonic zone was identified there. At Piton de la Fournaise in turn, we cannot rule out the existence of a paleo-surface composed of altered material, that would, locally, behave with such a weak effective friction. The alternative we advocate here invokes transient hydrothermal fluid pressurization associated with magma injections as proposed by Iverson (1995) and Reid (2004), and which dynamically reduces the effective normal stress throughout the domain, but not its intrinsic friction.

6.2. Implications on flank stability at Piton de la Fournaise

Now we discus our results in terms of flank stability with respect to previous studies :

1. First looking at superficial structures, Merle et al. (2010) showed from field observations the strong action of erosion in excavating deep canyons in lava flow ancient calderas bordering the external slopes south-west of Piton de la Fournaise (along the rivers canyons des Remparts and Langevin). Two large landslides are documented to have occurred there about 300 kyr and 150 kyr ago, and which would have carried away the entire southern flank of the preceding caldera. We note that this area in our models still hosts large plastic deformation, related to its steep topography. It remains prone to destabilization, perhaps facilitating punctually, magma pathways to bypass the Enclos Fouqué's morphological boundary and erupt via this south-westward depression (Merle et al., 2010). Our other observation of tensile failure upstream of the Rivière de l'Est is consistent with the occurrence of recurrent episodes of failures in this area (OVPF monthly bulletin, ISSN2610-5101, 2020).
2. The altered and hydrated first hundred meters could have been accounted for with a softer rheology in our models, as they play an important role upon slope stability over that same thickness, and on the occurrence of phreato-magmatic eruptions. Instead here we focused on quantifying the effective friction, which controls the failure yield at greater depth. At Piton de la Fournaise, a recent airborne electromagnetic survey reveals the first ca. 500 m depth resistivity structure of the edifice (Dumont et al., 2019). It highlights the upwelling hydrothermal system below the craters, magma injection pathways and mapped fault structures. Assessing the mechanical state of this 'superficial' level requires to adjust tensile strength and cohesion at these depths, in a way similar to other studies of non-volcanic, altered slopes such as for instance the Clapière landslide in France (Bouissou et al., 2012).
3. Michon et al. (2009, 2015) carried an extensive analysis of the faults and fractures that cover the Piton de la Fournaise area, questioning the role of pre-existing preferential orientations on the trajectories of magma injection. On the origin of the radial eruptive fissures oriented ca. N150 and N55 (Fig. **D.1**), Carter et al. (2007) argued that these are fracture zones that accommodate the eastern flank sliding, whereas Michon et al. (2009) proposed a predominant control from magma injection from below. In our models here, we see that in either cases whether we account for a dike injection or inflation of the magma reservoir, eccentric (radial) shear zones develop at the surface of the model and merge downslope: these eccentric shear zones have a natural curved (radial) shape in 3 dimensions that results from the 3D geometrical setting, as already discussed in section 5.3.
4. Michon et al. (2009, 2015) also discussed the potential link of the NE-SE rift zones with the motion of the eastern flank, and proposed a dynamic switch mechanism of tensile stresses rotating from vertical with deep vertical intrusions in the NE-SE rift zones, to horizontal when the magma propagates as sills below the eastern flank (then acting as a decollement zone, cf. Chaput et al., 2014). Our models here reproduce shear strain along a SE orientation resembling the SE rift zone, but nothing to the NE. This may mean that we would have to account in our models for additional specific deep heterogeneities or injection sources located below this NE rift zone. In other words, while the NE rift zone does not

link with any modeled feature, the SE rift zone may be attributed to an arm of deformation acting as a geometrical "extension" of the eastern flank shear zone. Further investigations are needed to determine accurately the potential for flank instabilities and eruptions pathways in this southern area above Saint-Philippe town.

5. Rincón et al. (2018) showed with analogue modeling that distinct deformation patterns could be induced depending on the location of a deep magma injection : a basal injection at the center below the edifice's summit induces summit subsidence (as observed in our models here for cases I2) and minor lateral sliding of a flank, leading to a relatively stable mechanical state with no catastrophic eruptions. In contrast an injection offset from the summit can induce a large flank gravitational collapse, with potentially triggered eruptions if the flank-slide intersects the injected magma. Such a scenario at Piton de la Fournaise would probably be tracked by a seismic sequence propagating upwards below the eastern flank and from greater depth than what is observed today.
6. A number of studies since the 1990s have explored the concept of the "Factor of Safety" to assess the stability of volcanic edifice flanks (e.g. Iverson, 1995; Reid, 2004; Apuani and Corazzato, 2009). As mentioned in the introduction, studies concluded in general that only relatively superficial landslides < 500m thick could occur, more superficial than the ca. >2 km thick slice that would be mobilized if it rooted on the observed cup-shape seismicity at Piton de la Fournaise. While these studies assume low magma overpressure (≤ 3 MPa) and high rock mass friction ($\geq 30°$), they invoke the key factor of rock mass effective strength reduction by transient thermally-pressurized fluid flow associated with a magma intrusion. Reid (2004) argued that the pressure wave propagates via the pores of the bedrock and cancels out the normal lithostatic stress component, hence reducing its effective friction. This would allow for destabilization of the flank slopes down deeper. Nevertheless in Reid's model, this pressure wave propagates rather quickly over a characteristic time of about 1 year. At Piton de la Fournaise, the persistent seismicity below the eastern flank has been recorded for much longer, ca. 30 yrs (Hirn et al., 1991). Hence, if one considers that magma reservoir overpressure is persistent over time, then it may induce a permanent overpressurized fluid flow throughout the bedrock that weakens it on the long-term. Further modelling of this transient phenomena, coupled to the eastern flank motion, would be useful. Actually, the fact that we could assimilate the observed seismicity *cup* with a shear zone by considering effective bedrock frictions as low as 3° or 5° is coincidentally indicative of a reduction in effective strength at the edifice's scale on the long-term.
7. A large flank slide is expected to begin with motion and uplift at its toe extremity (Iverson and Reid, 1992) (e.g. as is actually observed in Kilaua, Poland et al., 2017). Iverson and Reid (1992) showed that hydrothermal fluid flow actually accumulates there and has the strongest weakening effect, facilitating bedrock failure there. Such uplift is not measured by GPS on the eastern coastline of Piton de la Fournaise at present-day. In our models, only model M01 (Fig. 6a) with topography alone and

extremely weak bedrock displays such an uplift further to the east 5 km away below the coastline. Our other models with an inflating magma source do not produce an uplift (Figs. 7 and 8). The kinematic alternative is that flank sliding occurs horizontally along a flat lying decollement zone at depth $z \sim -2$ km extending further east below sea level : then horizontal motion would not necessarily have to be associated with toe uplift (e.g. Chaput et al., 2014). Measurements of slope motion offshore would help clarifying this point, but such data is not available yet.

8. Chaput et al. (2014) tested with numerical models the impact of a sill injected along a subhorizontal detachment identified to the north-east flank of the nearby Piton des Neiges. By assuming zero friction along this detachment plane and an overpressure of several MPa, they reproduced surface displacement patterns of several centimeters over a greater extent than if that detachment plane was frictional. Comparison to the measured surface displacements at Piton de la Fournaise led these authors to propose the existence of a magma-filled detachment zone below the eastern flank. They considered a bedrock with Young modulus 70 GPa, friction angle 30° and cohesion 4 MPa; it would be interesting to reassess these results with lower shear modulus and friction angle : the resulting surface displacements would overall be enhanced, hence the presence of frictionless magmatic material within the detachment might not be necessary. Such a decollement would then extend way down below sea level to the east, and as mentioned above, seismicity or ground motion should then be tracked there.
9. While our results show that the spatial distribution of seismicity can be explained by pressurization of the magma reservoir, they do not explain the temporal link between flank seismicity and the occurrence of lateral magma intrusions below the eastern flank (Figs. **10**, **D.2**). At Kilauea and Etna volcanoes for instance, it was shown that fault slip under the edifice flank coincides with dyking episodes (Delaney et al., 1990; Puglisi et al., 2008). Famin and Michon (2010) also suggested the role of sill intrusions in inducing flank destabilization at the nearby Piton des Neiges. At Piton de la Fournaise, detailed analysis of lateral injections that triggered abundant seismicity under the eastern flank of Piton de la Fournaise in 2020 and 2021 appear essential to better decipher this relationship: are these lateral intrusions generating the seismicity at depth or is it the motion of the eastern flank that favorizes their emplacement there ? Our models here indicate at least that lateral intrusions are not required to trigger the observed seismicity below the Eastern flank (section 5.3). On the other hand, the temporal relationship between eastern flank seismic shear mobilization and reservoir inflation is hinted by typical observations indicating first, long-lasting inflation and seismicity increase below the volcano summit (linked to reservoir pressurization), then followed by short-term intense seismic swarms and preferential motion towards the Eastern flank (linked with final propagation of magma to the surface).

7. Conclusion

Our numerical models illustrate first that the topographic gradient has a first order control on the stress field and deformation patterns at Piton de la Fournaise. It mobilizes potential surface displacements over several tens of meters. A minimum *effective* strength is deduced (*effective* friction is distinguished here from standard friction), that indicates how the edifice's shape can be maintained when not considering its anisotropic properties nor magma overpressure.

When exploring in a second step the influence of magma pressurization, the models show the development of a plastic shear zone of comparable cup-shape to that of the measured persistent seismicity along the eastern flank and dipping down to ca. $z = -2$ km, when the inflating source has a similar shape to the inferred shallow reservoir identified below Piton de la Fournaise (e.g. an ellipsoid source located at ca. $z = 0$ km depth). In contrast a shallower vertical intrusion below the eastern flank of the edifice produces a shallower plastic shear zone, not exceeding $z \sim -1$ km depth. Hence, we interpret the observed seismic *cup* as highlighting this persistent combination between gravitational and magmatic loading, without needing to prescribe any specific weakened behavior in this location. Furthermore in our models, increasing magma overpressure does not induce a large-scale flank-slide, indicating that this trigger alone, is not sufficient. The lack of observed uplift at the toe of the eastern flank supports this conclusion. We deduce that large-scale flank destabilization rooting at 2 km *bsl* would rather be triggered by another magma source specifically located below the eastern flank, a scenario not yet supported by present day observations.

Our models also indicate that the observed seismic cup is not necessarily a weakened structure storing magmatic fluids, although the low effective friction that was required to reproduce it calls for some hydrothermal transient fluid flow (that reduces the effective normal stress and allows for shear failure in that location). This does not exclude previous suggestions that this persistent seismicity illuminates the boundaries between altered and more rigid bodies at depth. While our models show that the depth of the plastic shear zone increases when the (effective) friction angle decreases, one should also bear in mind that the depth location of this seismic cup directly depends on the seismic velocities model (hence upon the Young's modulus). In order to gain further insight on the stability of the eastern flank of Piton de la Fournaise, further geophysical studies are required to assess the mechanical properties of the edifice.

Code and data availability: Seimic and GNSS data from Observatoire Volcanologique du Piton de la Fournaise are available on the volobsis website: `http://volobsis.ipgp.fr/`. Numerical models were achieved with the open-source code ADELI, which is available upon request to authors MG or RH, an old version with input files can be downloaded from `https://code.google.com/archive/p/adeli/`.

Competing interests: None of the authors express financial nor scientific conflicts of interest in this contribution.

Acknowledgements: This work was supported by the Agence Nationale de la Recherche, project No. ANR-16-CE04-0004-01 (SlideVOLC), by CNRS INSU Tellus-Aléas and Syster programs 2019, 2020; France. Z. Duputel aknowledges

757 support from the European Research Council (ERC) under grant agreement No. 805256. Colleagues and visitors
758 at OVPF are thanked for discussions. The models were ran on the OMP community cluster Nuwa (www.aero.obs-
759 mip.fr/parc-instru/platmod). We thank Susan Ellis and Diana Roman, for constructive and insightful reviews.

References

Annen, C., Sparks, R., 2002. Effects of repetitive emplacement of basaltic intrusions on thermal evolution and melt generation in the crust. Earth Planet. Sci. Lett. 203, 937–955.

Apuani, T., Corazzato, C., 2009. Numerical model of the stromboli volcano (italy) including the effect of magma pressure in the dyke system. Rock Mechanics and Rock Engineering 42, 53–72.

Apuani, T., Corazzato, C., Cancelli, A., Tibaldi, A., 2005. Stability of a collapsing volcano (stromboli, italy): Limit equilibrium analysis and numerical modelling. J. Volcano. Geotherm. Res. 144, 191–210.

Bachèlery, P., 1981. Le Piton de la Fournaise, Ile de la Réunion: étude volcanologique, structurale et pétrologique. Ph.D. thesis. Impr. UER Sci., France.

Barde-Cabusson, S., Finizola, A., Peltier, A., Chaput, M., Taquet, N., Dumont, S., Duputel, Z., Guy, A., Mathieu, L., Saumet, S., et al., 2012. Structural control of collapse events inferred by self-potential mapping on the piton de la fournaise volcano (la réunion island). J. Volcano. Geotherm. Res. 209, 9–18.

Battaglia, J., Ferrazzini, V., Staudacher, T., Aki, K., Cheminée, J.L., 2005. Pre-eruptive migration of earthquakes at the piton de la fournaise volcano (réunion island). Geophys. J. Int. 161, 549–558.

Beauducel, F., Peltier, A., Villié, A., Suryanto, W., 2020. Mechanical imaging of a volcano plumbing system from gnss unsupervised modeling. Geophys. Res. Int. 47, e2020GL089419.

Bonaccorso, A., Cianetti, S., Giunchi, C., Trasatti, E., Bonafede, M., Boschi, E., 2005. Analytical and 3-d numerical modelling of mt. etna (italy) volcano inflation. Geophys. J. Int. 163, 852–862.

Bonali, F.L., Corazzato, C., Tibaldi, A., 2011. Identifying rift zones on volcanoes: an example from la réunion island, indian ocean. Bulletin of volcanology 73, 347–366.

Boudoire, G., Liuzzo, M., Di Muro, A., Ferrazzini, V., Michon, L., Grassa, F., Derrien, A., Villeneuve, N., Bourdeu, A., Brunet, C., Giudice, G., Gurrieri, S., 2017. Investigating the deepest part of a volcano plumbing system: Evidence for an active magma path below the western flank of piton de la fournaise (la réunion island). J. Volcano. Geotherm. Res. 341, 193-–207.

Bouissou, S., Darnault, R., Chemenda, A., Rolland, Y., 2012. Evolution of gravity-driven rock slope failure and associated fracturing: Geological analysis and numerical modelling. Tectonophysics 526, 157–166.

Brenguier, F., Kowalski, P., Staudacher, T., Ferrazzini, V., Lauret, F., Boissier, P., Catherine, P., Lemarchand, A., Pequegnat, C., Meric, O., et al., 2012. First results from the undervolc high resolution seismic and gps network deployed on piton de la fournaise volcano. Seismological Res. Lett. 83, 97–102.

Brocher, T.M., 2005. Empirical relations between elastic wavespeeds and density in the earth's crust. Bulletin of the seismological Society of America 95, 2081–2092.

Carter, A., de Vries, B.v.W., Kelfoun, K., Bachèlery, P., Briole, P., 2007. Pits, rifts and slumps: the summit structure of piton de la fournaise. Bulletin of Volcanology 69, 741–756.

Cayol, V., Cornet, F.H., 1998. Three-dimensional modeling of the 1983–1984 eruption at piton de la fournaise volcano, réunion island. J. Geophys. Res.: Solid Earth 103, 18025–18037.

Cerpa, N.G., Araya, R., Gerbault, M., Hassani, R., 2015. Relationship between slab dip and topography segmentation in an oblique subduction zone: Insights from numerical modeling. Geophys. Res. Int. 42, 5786–5795.

Chaput, M., Pinel, V., Famin, V., Michon, L., Froger, J.L., 2014. Cointrusive shear displacement by sill intrusion in a detachment: A numerical approach. Geophys. Res. Int. 41, 1937–1943.

Chéry, J., Zoback, M.D., Hassani, R., 2001. An integrated mechanical model of the san andreas fault in central and northern california. J. Geophys. Res.: Solid Earth 106, 22051–22066.

Chevallier, L., Bachèlery, P., 1981. Evolution structurale du volcan actif du piton de la fournaise, ile de la réunion—océan indien occidental. Bulletin volcanologique 44, 723–741.

Chevrel, M.O., Favalli, M., Villeneuve, N., Harris, A.J., Fornaciai, A., Richter, N., Derrien, A., Boissier, P., di Muro, A., Peltier, A., 2021. Lava flow hazard map of piton de la fournaise volcano. Nat. Hazards Earth Sys. Sci. 21, 2355–2377.

Cocco, M., Rice, J.R., 2002. Pore pressure and poroelasticity effects in coulomb stress analysis of earthquake interactions. J. Geophys. Res.: Solid Earth 107, ESE–2.

Collettini, C., Tesei, T., Scuderi, M.M., Carpenter, B.M., Viti, C., 2019. Beyond byerlee friction, weak faults and implications for slip behavior. Earth Planet. Sci. Lett. 519, 245–263.

Cundall, P., 1988. A microcomputer program for modeling large-strain plasticity problems. Numerical Methods in Geomechanics (Innsbruck 1988) , 2101–2108.

Currenti, G., Williams, C.A., 2014. Numerical modeling of deformation and stress fields around a magma chamber: Constraints on failure conditions and rheology. Physics of the Earth and Planetary Interiors 226, 14–27.

De Barros, L., Baques, M., Godano, M., Helmstetter, A., Deschamps, A., Larroque, C., Courboulex, F., 2019. Fluid-induced swarms and coseismic stress transfer: A dual process highlighted in the aftershock sequence of the 7 april 2014 earthquake (ml 4.8, ubaye, france). J. Geophys. Res.: Solid Earth 124, 3918–3932.

Delaney, P.T., Fiske, R.S., Miklius, A., Okamura, A.T., Sako, M.K., 1990. Deep magma body beneath the summit and rift zones of kilauea volcano, hawaii. Science 247, 1311–1316.

Di Muro, A., Métrich, N., Vergani, D., Rosi, M., Armienti, P., Fougeroux, T., Deloule, E., Arienzo, I., Civetta, L., 2014. The shallow plumbing system of piton de la fournaise volcano (la reunion island, indian ocean) revealed by the major 2007 caldera-forming eruption. J. Petrology 55, 1287–1315.

Dorbath, C., Gerbault, M., Carlier, G., Guiraud, M., 2008. Double seismic zone of the nazca plate in northern chile: High-resolution velocity structure, petrological implications, and thermomechanical modeling. Geochem. Geophys. Geosys. 9.

Driad, L., 1997. Structure profonde de l'édifice volcanique de La Réunion (océan Indien) par sismique réfraction et grand angle. Ph.D. thesis. Paris 7.

Dumont, M., Peltier, A., Roblin, E., Reninger, P.A., Barde-Cabusson, S., Finizola, A., Ferrazzini, V., 2019. Imagery of internal structure and destabilization features of active volcano by 3d high resolution airborne electromagnetism. Sci. reports 9, 1–11.

Dumont, Q., Cayol, V., Froger, J.L., Peltier, A., 2022. 22 years of satellite imagery reveal a major destabilization structure at piton de la fournaise. Nature Comm. 13, 1–11.

Duputel, Z., Ferrazzini, V., Lengliné, O., Michon, L., Fontaine, F.R., Massin, F., 2021. Seismicity of la réunion island. Comptes Rendus Géoscience 353, 1–19.

Duputel, Z., Lengliné, O., Ferrazzini, V., 2019. Constraining spatiotemporal characteristics of magma migration at piton de la fournaise volcano from pre-eruptive seismicity. Geophys. Res. Lett. 46, 119–127.

Ernst, R., Head, J., Parfitt, E., Grosfils, E., Wilson, L., 1995. Giant radiating dyke swarms on earth and venus. Earth-Science Reviews 39, 1–58.

Famin, V., Michon, L., 2010. Volcano destabilization by magma injections in a detachment. Geology 38, 219–222.

Fontaine, F.R., Barruol, G., Tkalčić, H., Wölbern, I., Rümpker, G., Bodin, T., Haugmard, M., 2015. Crustal and uppermost mantle structure variation beneath la réunion hotspot track. Geophys. J. Int. 203, 107–126.

Froger, J.L., Famin, V., Cayol, V., Augier, A., Michon, L., Lénat, J.F., 2015. Time-dependent displacements during and after the april 2007 eruption of piton de la fournaise, revealed by interferometric data. J. Volcano. Geotherm. Res. 296, 55–68.

Fukushima, Y., Cayol, V., Durand, P., 2005. Finding realistic dike models from interferometric synthetic aperture radar data: The february 2000 eruption at piton de la fournaise. J. Geophys. Res.: Solid Earth 110.

Fukushima, Y., Cayol, V., Durand, P., Massonnet, D., 2010. Evolution of magma conduits during the 1998–2000 eruptions of piton de la fournaise volcano, réunion island. J. Geophys. Res.: Solid Earth 115.

Gailler, L.S., Martí, A., Lénat, J.F., 2018. Complex structure of piton de la fournaise and its underlying lithosphere revealed

by magnetotelluric 3d inversion. J. Volcano. Geotherm. Res. 356, 200–210.

Gallart, J., Driad, L., Charvis, P., Sapin, M., Hirn, A., Diaz, J., de Voogd, B., Sachpazi, M., 1999. Perturbation to the lithosphere along the hotspot track of la réunion from an offshore-onshore seismic transect. J. Geophys. Res.: Solid Earth 104, 2895–2908.

Gerbault, M., Cappa, F., Hassani, R., 2012. Elasto-plastic and hydromechanical models of failure around an infinitely long magma chamber. Geochem. Geophys. Geosys. 13.

Gerbault, M., Fontaine, F.J., Rabinowicz, M., Bystricky, M., 2017. Elastic flexure controls magma trajectories and explains the offset of primary volcanic activity upstream of mantle plume axis at la réunion and hawaii hotspot islands. Earth Planet. Sci. Lett. 462, 142–156.

Gerbault, M., Hassani, R., Novoa Lizama, C., Souche, A., 2018. Three-dimensional failure patterns around an inflating magmatic chamber. Geochem. Geophys. Geosys. 19, 749–771.

Gerbault, M., Henrys, S., Davey, F., 2003. Numerical models of lithospheric deformation forming the southern alps of new zealand. J. Geophys. Res.: Solid Earth 108.

Gerbault, M., Poliakov, A.N., Daignieres, M., 1998. Prediction of faulting from the theories of elasticity and plasticity: what are the limits? Journal of Structural Geology 20, 301.

Geuzaine, C., Remacle, J.F., 2009. Gmsh: A 3-d finite element mesh generator with built-in pre-and post-processing facilities. International journal for numerical methods in engineering 79, 1309–1331.

Gillot, P.Y., Lefèvre, J.C., Nativel, P.E., 1994. Model for the structural evolution of the volcanoes of réunion island. Earth Planet. Sci. Lett. 122, 291–302.

Gillot, P.Y., Nativel, P., 1989. Eruptive history of the piton de la fournaise volcano, réunion island, indian ocean. J. Volc. Geotherm. Res. 36, 53–65.

Ginouves, J.R., Gerbault, M., Cembrano, J., Iturrieta, P., Leiva, F.S., Novoa, C., Hassani, R., 2021. The interplay of a fault zone and a volcanic reservoir from 3d elasto-plastic models: Rheological conditions for mutual trigger based on a field case from the andean southern volcanic zone. J. Volcano. Geotherm. Res. , 107317.

Got, J.L., Amitrano, D., Stefanou, I., Brothelande, E., Peltier, A., 2019. Damage and strain localization around a pressurized shallow-level magma reservoir. J. Geophys. Res.: Solid Earth 124, 1443–1458.

Got, J.L., Carrier, A., Marsan, D., Jouanne, F., Vogfjörd, K., Villemin, T., 2017. An analysis of the nonlinear magma-edifice coupling at grimsvötn volcano (iceland). J. Geophys. Res.: Solid Earth 122, 826–843.

Got, J.L., Fréchet, J., Klein, F.W., 1994. Deep fault plane geometry inferred from multiplet relative relocation beneath the south flank of kilauea. J. Geophys. Res.: Solid Earth 99, 15375–15386.

Got, J.L., Monteiller, V., Monteux, J., Hassani, R., Okubo, P., 2008. Deformation and rupture of the oceanic crust may control growth of hawaiian volcanoes. Nature 451, 453–456.

Got, J.L., Peltier, A., Staudacher, T., Kowalski, P., Boissier, P., 2013. Edifice strength and magma transfer modulation at piton de la fournaise volcano. J. Geophys. Res.: Solid Earth 118, 5040–5057.

Gudmundsson, A., 2006. How local stresses control magma-chamber ruptures, dyke injections, and eruptions in composite volcanoes. Earth-Science Reviews 79, 1–31.

Hassani, R., Jongmans, D., Chéry, J., 1997. Study of plate deformation and stress in subduction processes using two-dimensional numerical models. J. Geophys. Res.: Solid Earth 102, 17951–17965.

Havlin, C., Parmentier, E., Hirth, G., 2013. Dike propagation driven by melt accumulation at the lithosphere–asthenosphere boundary. Earth Planet. Sci. Lett. 376, 20–28.

Heap, M.J., Villeneuve, M., Albino, F., Farquharson, J.I., Brothelande, E., Amelung, F., Got, J.L., Baud, P., 2020. Towards more realistic values of elastic moduli for volcano modelling. J. Volc. Geotherm. Res. 390, 106684.

Hirn, A., Lépine, J.C., Sapin, M., Laigle, M., Nicolich, R., Gallart, J., Lankar, V., Nercessian, A., Voogd, B., Charvis, P.,

et al., 1999. Structure interne du piton de la fournaise et de l'etna d'apres la tomographie sismique. Rapport Quadriennal 1995-1998 CNFGG , 129–136.

Hirn, A., Lépine, J.C., Sapin, M., H., D., 1991. Episodes of pit-crater collapse documented by seismology at piton de la fournaise. J. Volcano. Geotherm. Res. 47, 89-104.

Holohan, E.P., Walter, T.R., Schöpfer, M.P., Walsh, J.J., van Wyk de Vries, B., Troll, V.R., 2013. Origins of oblique-slip faulting during caldera subsidence. J. Geophys. Res.: Solid Earth 118, 1778–1794.

Hurwitz, D.M., Long, S.M., Grosfils, E.B., 2009. The characteristics of magma reservoir failure beneath a volcanic edifice. J. Volcano. Geotherm. Res. 188, 379–394.

Iverson, R.M., 1995. Can magma-injection and groundwater forces cause massive landslides on hawaiian volcanoes? J. Volcano. Geotherm. Res. 66, 295–308.

Iverson, R.M., Reid, M.E., 1992. Gravity-driven groundwater flow and slope failure potential: 1. elastic effective-stress model. Water Resources Research 28, 925–938.

Jaeger, J.C., Cook, N., 1979. Fundamentals of rock mechanics, Third edition. London: Chapman and Hall.

King Hubbert, M., Rubey, W.W., 1959. Role of fluid pressure in mechanics of overthrust faulting: I. mechanics of fluid-filled porous solids and its application to overthrust faulting. Geol. Soc. Am. Bull. 70, 115–166.

Lengliné, O., Duputel, Z., Ferrazzini, V., 2016. Uncovering the hidden signature of a magmatic recharge at piton de la fournaise volcano using small earthquakes. Geophys. Res. Int. 43, 4255–4262.

Leroy, Y., Ortiz, M., 1989. Finite element analysis of strain localization in frictional materials. International journal for numerical and analytical methods in geomechanics 13, 53–74.

Lomax, A., Virieux, J., Volant, P., Berge-Thierry, C., 2000. Probabilistic earthquake location in 3d and layered models, in: Advances in Seismic Event Location. Springer, Dordrecht, pp. 101–134. doi:10.1007/978-94-015-9536-0-5.

Masterlark, T., 2007. Magma intrusion and deformation predictions: Sensitivities to the mogi assumptions. J. Geophys. Res.: Solid Earth 112.

McDougall, I., 1971. The geochronology and evolution of the young volcanic island of réunion, indian ocean. Geochimica et Cosmochimica Acta 35, 261–288.

Merle, O., Mairine, P., Michon, L., Bachèlery, P., Smietana, M., 2010. Calderas, landslides and paleo-canyons on piton de la fournaise volcano (la réunion island, indian ocean). J. Volcano. Geotherm. Res. 189, 131–142.

Michon, L., Cayol, V., Letourneur, L., Peltier, A., Villeneuve, N., Staudacher, T., 2009. Edifice growth, deformation and rift zone development in basaltic setting: Insights from piton de la fournaise shield volcano (réunion island). J. Volc. Geotherm. Res. 184, 14–30.

Michon, L., Ferrazzini, V., Di Muro, A., Villeneuve, N., Famin, V., 2015. Rift zones and magma plumbing system of piton de la fournaise volcano: How do they differ from hawaii and etna? J. Volcano. Geotherm. Res. 303, 112–129.

Michon, L., Saint-Ange, F., 2008. Morphology of piton de la fournaise basaltic shield volcano (la réunion island): Characterization and implication in the volcano evolution. J. Geophys. Res.: Solid Earth 113.

Morgan, J.K., McGovern, P.J., 2005a. Discrete element simulations of gravitational volcanic deformation: 1. deformation structures and geometries. J. Geophys. Res.: Solid Earth 110.

Morgan, J.K., McGovern, P.J., 2005b. Discrete element simulations of gravitational volcanic deformation: 2. mechanical analysis. J. Geophys. Res.: Solid Earth 110.

Nádai, A., 1963. Theory of Flow and Fracture of Solids; Volume 2. New York, NY, McGraw-Hill Book Company Incorporated.

Novoa, C., Remy, D., Gerbault, M., Baez, J., Tassara, A., Cordova, L., Cardona, C., Granger, M., Bonvalot, S., Delgado, F., 2019. Viscoelastic relaxation: A mechanism to explain the decennial large surface displacements at the laguna del maule silicic volcanic complex. Earth Planet. Sci. Lett. 521, 46–59.

Oehler, J.F., Lénat, J.F., Labazuy, P., 2008. Growth and collapse of the reunion island volcanoes. Bulletin of Volcanology 70,

717–742.

Peltier, A., Bachèlery, P., Staudacher, T., 2009. Magma transport and storage at piton de la fournaise (la réunion) between 1972 and 2007: A review of geophysical and geochemical data. J. Volcano. Geotherm. Res. 184, 93–108.

Peltier, A., Famin, V., Bachèlery, P., Cayol, V., Fukushima, Y., Staudacher, T., 2008. Cyclic magma storages and transfers at piton de la fournaise volcano (la réunion hotspot) inferred from deformation and geochemical data. Earth Planet. Sci. Lett. 270, 180–188.

Peltier, A., Got, J.L., Villeneuve, N., Boissier, P., Staudacher, T., Ferrazzini, V., Walpersdorf, A., 2015. Long-term mass transfer at piton de la fournaise volcano evidenced by strain distribution derived from gnss network. J. Geophys. Res.: Solid Earth 120, 1874–1889.

Peltier, A., Staudacher, T., Catherine, P., Ricard, L.P., Kowalski, P., Bachèlery, P., 2006. Subtle precursors of volcanic eruptions at piton de la fournaise detected by extensometers. Geophysical research letters 33.

Pinel, V., Jaupart, C., 2005. Caldera formation by magma withdrawal from a reservoir beneath a volcanic edifice. Earth Planet. Sci. Lett. 230, 273–287.

Pinel, V., Jaupart, C., Albino, F., 2010. On the relationship between cycles of eruptive activity and growth of a volcanic edifice. J. Volcano. Geotherm. Res. 194, 150–164.

Poland, M.P., Peltier, A., Bonforte, A., Puglisi, G., 2017. The spectrum of persistent volcanic flank instability: A review and proposed framework based on kīlauea, piton de la fournaise, and etna. J. Volcano. Geotherm. Res. 339, 63–80.

Poliakov, A., Cundall, P., Podladchikov, Y., Lyakhovsky, V., 1993. An explicit inertial method for the simulation of viscoelastic flow: an evaluation of elastic effects on diapiric flow in two-and three-layers models, in: Flow and Creep in the Solar System: observations, modeling and Theory. Springer, Dordrecht, pp. 175–195.

Prôno, E., Battaglia, J., Monteiller, V., Got, J.L., Ferrazzini, V., 2009. P-wave velocity structure of piton de la fournaise volcano deduced from seismic data recorded between 1996 and 1999. J. Volcano. Geotherm. Res. 184, 49–62.

Puglisi, G., Bonforte, A., Ferretti, A., Guglielmino, F., Palano, M., Prati, C., 2008. Dynamics of mount etna before, during, and after the july–august 2001 eruption inferred from gps and differential synthetic aperture radar interferometry data. J. Geophys. Res.: Solid Earth 113.

Reid, M.E., 2004. Massive collapse of volcano edifices triggered by hydrothermal pressurization. Geology 32, 373–376.

Rincón, M., Márquez, A., Herrera, R., Alonso-Torres, A., Granja-Bruña, J.L., de Vries, B.v.W., 2018. Contrasting catastrophic eruptions predicted by different intrusion and collapse scenarios. Scientific reports 8, 1–11.

Roult, G., Peltier, A., Taisne, B., Staudacher, T., Ferrazzini, V., Di Muro, A., et al., 2012. A new comprehensive classification of the piton de la fournaise activity spanning the 1985–2010 period. search and analysis of short-term precursors from a broad-band seismological station. J. Volcano. Geotherm. Res. 241, 78–104.

Saffer, D.M., Marone, C., 2003. Comparison of smectite-and illite-rich gouge frictional properties: application to the updip limit of the seismogenic zone along subduction megathrusts. Earth Planet. Sci. Lett. 215, 219–235.

Sartoris, G., Pozzi, J., Philippe, C., Le Moüel, J., 1990. Mechanical stability of shallow magma chambers. J. Geophys. Res. Solid Earth 95, 5141–5151.

Sibson, R.H., 1994. Crustal stress, faulting and fluid flow. Geological Society, London, Special Publications 78, 69–84.

Simo, J., Kennedy, J., Govindjee, S., 1988. Non-smooth multisurface plasticity and viscoplasticity. loading/unloading conditions and numerical algorithms. Int. J. Num. Meth. Engineering 26, 2161–2185.

Smittarello, D., Cayol, V., Pinel, V., Peltier, A., Froger, J.L., Ferrazzini, V., 2019. Magma propagation at piton de la fournaise from joint inversion of insar and gnss. J. Geophys. Res.: Solid Earth 124, 1361–1387.

Staudacher, T., Ferrazzini, V., Peltier, A., Kowalski, P., Boissier, P., Catherine, P., Lauret, F., Massin, F., 2009. The april 2007 eruption and the dolomieu crater collapse, two major events at piton de la fournaise (la réunion island, indian ocean). J. Volcano. Geotherm. Res. 184, 126–137.

974 Suppe, J., 2014. Fluid overpressures and strength of the sedimentary upper crust. Journal of Structural Geology 69, 481–492.
975 Terzaghi, K., 1943. Theoretical soil mechanics. J. Wiley & sons, New York.
976 Timoshenko, S.P., Goodier, J.N., 1951. Theory of elasticity. McGraw-Hill, New York.
977 Trasatti, E., Giunchi, C., Bonafede, M., 2003. Effects of topography and rheological layering on ground deformation in volcanic
978 regions. J. Volcano. Geotherm. Res. 122, 89–110.
979 Trasatti, E., Giunchi, C., Bonafede, M., 2005. Structural and rheological constraints on source depth and overpressure estimates
980 at the campi flegrei caldera, italy. J. Volc. Geotherm. Res. 144, 105–118.
981 Traversa, P., Pinel, V., Grasso, J., 2010. A constant influx model for dike propagation: Implications for magma reservoir
982 dynamics. J. Geophys. Res.: Solid Earth 115.
983 Tridon, M., Cayol, V., Froger, J.L., Augier, A., Bachèlery, P., 2016. Inversion of coeval shear and normal stress of piton de la
984 fournaise flank displacement. J. Geophys. Res.: Solid Earth 121, 7846–7866.
985 Villeneuve, M.C., Heap, M.J., Kushnir, A.R., Qin, T., Baud, P., Zhou, G., Xu, T., 2018. Estimating in situ rock mass strength
986 and elastic modulus of granite from the soultz-sous-forêts geothermal reservoir (france). Geothermal Energy 6, 1–29.
987 Watanabe, T., Masuyama, T., Nagaoka, K., Tahara, T., 2002. Analog experiments on magma-filled cracks: Competition
988 between external stresses and internal pressure. Earth, planets and space 54, e1247–e1261.
989 White, R.S., Drew, J., Martens, H.R., Key, J., Soosalu, H., Jakobsdóttir, S.S., 2011. Dynamics of dyke intrusion in the
990 mid-crust of iceland. Earth Planet. Sci. Lett. 304, 300–312.

Appendix A. Numerical integration of the constitutive law

The numerical integration of the elastoplastic Drucker-Prager constitutive model combined with a tensile failure criterion is described here. For sake of simplicity only the case of infinitesimal deformations is considered, and more details on the numerical method used in ADELI in the context of finite strain can be found in Chéry et al. (2001). A standard version of the code (in french) remains available here, `https://code.google.com/archive/p/adeli/`, and an updated version is available upon request (to MG or RH).

Appendix A.1. Yield functions, plastic potentials and flow rule

Following the general formulation given in Simo et al. (1988) for non-smooth multisurface plasticity and its numerical implementation, we consider, as in the Itasca Flac's manual, the special case where the set of plastically admissible stresses is the truncated cone:

$$\Omega = \left\{\boldsymbol{\sigma} \in \mathbb{R}^6 \mid f_s(\boldsymbol{\sigma}) \leq 0\right\} \cap \left\{\boldsymbol{\sigma} \in \mathbb{R}^6 \mid f_t(\boldsymbol{\sigma}) \leq 0\right\}, \tag{A.1}$$

with f_s the classical Drucker-Prager yield function and f_t the tension yield function:

$$f_s(\boldsymbol{\sigma}) = J(\boldsymbol{s}) + \alpha\,(p - p_0), \qquad f_t(\boldsymbol{\sigma}) = p - p_t, \tag{A.2}$$

where $p = \frac{1}{3}\mathrm{trace}(\boldsymbol{\sigma})$ is the mean stress, $J(\boldsymbol{s}) = \sqrt{\frac{3}{2}}\|\boldsymbol{s}\|$ the equivalent stress, $\boldsymbol{s} = \boldsymbol{\sigma} - p\,\boldsymbol{I}$ the deviatoric stress ($\|\boldsymbol{s}\| = \sqrt{\boldsymbol{s} : \boldsymbol{s}}$), $p_0 = c/\tan\varphi$, $\alpha = 6\sin\varphi/(3 - \sin\varphi)$, c the cohesion, φ the friction angle and p_t is the tensile strength (it is assumed in the following that $p_t \leq p_0$, the classical Drucker-Prager criterion corresponding to the particular case $p_t = p_0$). When isotropic harderning/softening phenomenon is considered, φ is a given function of the accumulated equivalent plastic strain $\int_0^t \sqrt{2/3}\|\dot{\boldsymbol{\varepsilon}}_p\|$ (Leroy and Ortiz, 1989).

To complete the formulation the evolution of the plastic strain rate is given by the flow rule

$$\dot{\boldsymbol{\varepsilon}}_p = \dot{\lambda}_s\,\frac{\partial g_s}{\partial \boldsymbol{\sigma}} + \dot{\lambda}_t\,\frac{\partial g_t}{\partial \boldsymbol{\sigma}}, \tag{A.3}$$

with g_s and g_t the two corresponding plastic potentials whose gradients are defined by :

$$\frac{\partial g_s}{\partial \boldsymbol{\sigma}} = \frac{3}{2}\frac{\boldsymbol{s}}{J(\boldsymbol{s})} + \frac{1}{3}\beta\,\boldsymbol{I}, \qquad \frac{\partial g_t}{\partial \boldsymbol{\sigma}} = \frac{1}{3}\boldsymbol{I}, \tag{A.4}$$

where $\beta = 6\sin\psi/(3 - \sin\psi)$ and ψ is the dilatancy angle (thus in this model the flow rule for tensile failure is associated while it is non-associated for shear failure unless $\varphi = \psi$).

In (A.3) $\dot{\lambda}_s$ and $\dot{\lambda}_t$ are two plastic multipliers which satisfy the complementary conditions:

$$\begin{aligned} &\dot{\lambda}_s \geq 0, \qquad f_s(\boldsymbol{\sigma}) \leq 0, \qquad \dot{\lambda}_s f_s(\boldsymbol{\sigma}) = 0, \\ &\dot{\lambda}_t \geq 0, \qquad f_t(\boldsymbol{\sigma}) \leq 0, \qquad \dot{\lambda}_t f_t(\boldsymbol{\sigma}) = 0. \end{aligned} \tag{A.5}$$

Appendix A.2. Elastic predictor / plastic corrector algorithm

For materials with linear isotropic elastic response, the elastoplatic incremental constitutive law, splitted for convenience in its deviatoric and volumetric parts, reads

$$\begin{cases} \dot{\boldsymbol{s}} = 2G\,(\dot{\boldsymbol{e}} - \dot{\boldsymbol{e}}_p), \\ \dot{p} = K\,(\dot{\bar{\varepsilon}} - \dot{\bar{\epsilon}}_p) \end{cases} \tag{A.6}$$

with G and K the shear modulus and the bulk modulus, respectively, $\dot{\boldsymbol{e}} = \mathrm{dev}(\dot{\boldsymbol{\varepsilon}})$ the deviatoric part of the total strain rate tensor $\dot{\boldsymbol{\varepsilon}}$, $\dot{\bar{\varepsilon}} = \mathrm{trace}(\dot{\boldsymbol{\varepsilon}})$, $\dot{\boldsymbol{e}}_p = \mathrm{dev}(\dot{\boldsymbol{\varepsilon}}_p)$ and $\dot{\bar{\varepsilon}}_p = \mathrm{trace}(\dot{\boldsymbol{\varepsilon}}_p)$.
Assuming a known constant strain-rate over the time step $[t^n, t^{n+1}]$, the integration of (A.6) using the implicit backward Euler scheme provides

$$\begin{cases} \boldsymbol{s}^{n+1} = \boldsymbol{s}_e - 2G\,\Delta\boldsymbol{e}_p^{n+1}, \\ p^{n+1} = p_e - K\,\Delta\bar{\varepsilon}_p^{n+1}, \end{cases} \tag{A.7}$$

where $\Delta\boldsymbol{e}_p^{n+1} = \Delta t\,\dot{\boldsymbol{e}}_p^{n+1}$ and $\Delta\bar{\varepsilon}_p^{n+1} = \Delta t\,\dot{\bar{\varepsilon}}_p^{n+1}$ are the deviatoric and volumetric plastic strain increments, respectively and

$$\begin{cases} \boldsymbol{s}_e := \boldsymbol{s}^n + 2G\Delta t\,\dot{\boldsymbol{e}}, \\ p_e := p^n + K\Delta t\,\dot{\bar{\varepsilon}}, \end{cases} \tag{A.8}$$

are known at the beginning of the time-step and correspond to the elastic prediction of the stress field.

If the predicted stress $\boldsymbol{\sigma}_e = \boldsymbol{s}_e + p_e\,\boldsymbol{I}$ lies within Ω, then the solution at t^{n+1} is obtained : $\boldsymbol{\sigma}^{n+1} = \boldsymbol{\sigma}_e$, $\dot{\boldsymbol{\varepsilon}}_p^{n+1} = \boldsymbol{0}$. Otherwise the prediction is not plastically admissible and $\boldsymbol{\sigma}_e$ must be projected onto the surface of Ω. To uniquely define this projection, one possible strategy is to first split the exterior of Ω into the following three complementary domains that may contain $\boldsymbol{\sigma}_e$ (see Figure A.1):

$$\Omega_t = \left\{\boldsymbol{\sigma} \in \mathbb{R}^6 \mid f_t(\boldsymbol{\sigma}) > 0,\ h_t(\boldsymbol{\sigma}) := J(\boldsymbol{s}) - J^* \leq 0\right\}, \tag{A.9}$$

where $J^* = \alpha\,(p_0 - p_t)$ is the radius of the terminal section of the truncated cone Ω,

$$\Omega_s = \left\{\boldsymbol{\sigma} \in \mathbb{R}^6 \mid f_s(\boldsymbol{\sigma}) > 0,\ h_s(\boldsymbol{\sigma}) := p_t - p + \beta\,h_t(\boldsymbol{\sigma}) > 0\right\}, \tag{A.10}$$

and

$$\Omega' = \left\{\boldsymbol{\sigma} \in \mathbb{R}^6 \mid h_s(\boldsymbol{\sigma}) \leq 0,\ h_t(\boldsymbol{\sigma}) > 0\right\}. \tag{A.11}$$

Then, depending on the domain in which $\boldsymbol{\sigma}_e$ is located, the plastic correction is defined as follows:

1) if $\boldsymbol{\sigma}_e \in \Omega_t$: the projection is done along the direction of the gradient of g_t. The plastic strain rate is therefore given by (A.3) with $\dot{\lambda}_s = 0$ and $\dot{\lambda}_t \geq 0$. Using equations (A.4) (which gives $\dot{\bar{\varepsilon}}_p = \dot{\lambda}_t$) and (A.7), the expression of $\dot{\lambda}_t$ follows from the consistency condition $f_t(\boldsymbol{\sigma}^{n+1}) = 0$:

$$\dot{\lambda}_t \Delta t = \frac{f_t(\boldsymbol{\sigma}_e)}{K}. \tag{A.12}$$

Hence, the plastic strain increment and the updated stress in this case are simply

$$\begin{array}{ll} \bullet\ \Delta\boldsymbol{e}_p^{n+1} = \boldsymbol{0} & \bullet\ \Delta\bar{\varepsilon}_p = \dot{\lambda}_t\Delta t \\ \bullet\ \boldsymbol{s}^{n+1} = \boldsymbol{s}_e & \bullet\ p^{n+1} = p_t \end{array} \tag{A.13}$$

2) if $\boldsymbol{\sigma}_e \in \Omega_s$: the projection is made along the direction of the gradient of g_s. The plastic strain rate is then given by (A.3) with $\dot{\lambda}_t = 0$ and $\dot{\lambda}_s \geq 0$ follows from the consistency condition $f_s(\boldsymbol{\sigma}^{n+1}) = 0$. Using (A.4) (which gives $\dot{\boldsymbol{e}}_p = \dot{\lambda}_s \frac{3\boldsymbol{s}}{2J}$ and $\dot{\bar{\varepsilon}}_p = \dot{\lambda}_s \beta$) and (A.7) and noting that $J(\boldsymbol{s}^{n+1}) = J(\boldsymbol{s}_e) - 3G\dot{\lambda}_s \Delta t$,in absence of hardening, this condition gives :

$$\dot{\lambda}_s \Delta t = \frac{f_s(\boldsymbol{\sigma}_e)}{3G + K\alpha\beta}. \tag{A.14}$$

Hence, the plastic strain increment and the updated stress in this case are

$$\begin{aligned} &\bullet\ \Delta \boldsymbol{e}_p^{n+1} = \tfrac{3\dot{\lambda}_s \Delta t}{2J(\boldsymbol{s}_e)}\, \boldsymbol{s}_e && \bullet\ \Delta \bar{\varepsilon}_p^{n+1} = \beta \dot{\lambda}_s \Delta t \\ &\bullet\ \boldsymbol{s}^{n+1} = \left(1 - \tfrac{3G\dot{\lambda}_s \Delta t}{J(\boldsymbol{s}_e)}\right) \boldsymbol{s}_e && \bullet\ p^{n+1} = p_e - K\beta\dot{\lambda}_s \Delta t \end{aligned} \tag{A.15}$$

It is worth noting that when hardening is allowed the consistency condition is a non-linear function of $\dot{\lambda}_s$ and it is generally no longer possible to have a closed-form such as (A.14) for $\dot{\lambda}_s$. In this case (A.14) can however be used as an initial guess of $\dot{\lambda}_s$ in an iterative procedure (the standard Newton method is used in Adeli).

3) if $\boldsymbol{\sigma}_e \in \Omega'$: the correction is achieved by projecting $\boldsymbol{\sigma}_e$ on the closest point of the terminal cone contour zone (see Figure A.1). Then $p^{n+1} = p_t$ and $\boldsymbol{s}^{n+1} = (J^*/J(\boldsymbol{s}_e))\, \boldsymbol{s}_e$. The plastic strain increment is obtained by injecting these values into (A.7). Hence,

$$\begin{aligned} &\bullet\ \Delta \boldsymbol{e}_p^{n+1} = \tfrac{1 - J^*/J(\boldsymbol{s}_e)}{2G}\, \boldsymbol{s}_e && \bullet\ \Delta \bar{\varepsilon}_p^{n+1} = \tfrac{p_e - p_t}{K} \\ &\bullet\ \boldsymbol{s}^{n+1} = \tfrac{J^*}{J(\boldsymbol{s}_e)}\, \boldsymbol{s}_e && \bullet\ p^{n+1} = p_t \end{aligned} \tag{A.16}$$

General remark: These four cases can be rewritten into the single form:

$$\begin{aligned} &\bullet\ \Delta \boldsymbol{e}_p = \zeta^{dev} \boldsymbol{s}_e / 2G && \bullet\ \Delta \bar{\varepsilon}_p = \zeta^{vol} p_e / K \\ &\bullet\ \boldsymbol{s}^{n+1} = (1 - \zeta^{dev})\, \boldsymbol{s}_e && \bullet\ p^{n+1} = (1 - \zeta^{vol})\, p_e \end{aligned} \tag{A.17}$$

with ζ^{dev} and ζ^{vol} two dimensionless numbers defined as follows:

$$\begin{aligned} &0) \text{ if } \boldsymbol{\sigma}_e \in \Omega_e : && \zeta^{dev} = 0, && \zeta^{vol} = 0, \\ &1) \text{ if } \boldsymbol{\sigma}_e \in \Omega_s : && \zeta^{dev} = 3G\dot{\lambda}\Delta t / J(\boldsymbol{s}_e), && \zeta^{vol} = K\beta\dot{\lambda}\Delta t / p_e, \\ &2) \text{ if } \boldsymbol{\sigma}_e \in \Omega_t : && \zeta^{dev} = 0, && \zeta^{vol} = 1 - p_t/p_e \\ &3) \text{ if } \boldsymbol{\sigma}_e \in \Omega' : && \zeta^{dev} = 1 - J^*/J(\boldsymbol{s}_e), && \zeta^{vol} = 1 - p_t/p_e. \end{aligned} \tag{A.18}$$

In perfect plasticity, $\dot{\lambda}\Delta t = f_s(\boldsymbol{\sigma}_e)/(3G + K\alpha\beta)$ otherwise is determined numerically as the root of $f_s(\boldsymbol{\sigma}^{n+1}(\dot{\lambda}\Delta t)) = 0$.

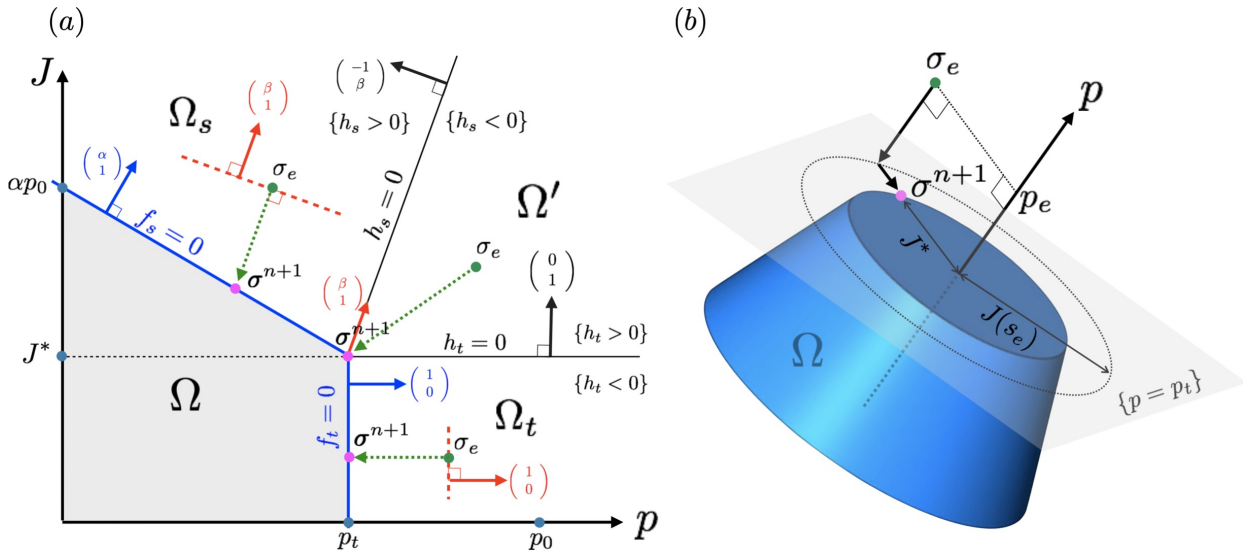

Figure A.1: Combined Drucker-Prager criterion and tensile failure criterion. (a) View in the p–J plane of the plastically admissible domain (Ω) and plastic corrections and their corresponding projections (green arrows) when the elastic prediction $\boldsymbol{\sigma}_e$ lies in Ω_s, Ω_t or Ω'. Gradients of the yield and potential functions are represented by blue and red arrows, respectively. h_s and h_t are defined in (A.10) and (A.9). (b) View in the principal stresses space and correction for $\boldsymbol{\sigma}_e \in \Omega'$.

Table A.3: Definition of main models parameters.

Symbol	meaning	values
E	Young modulus	10 GPa
T	Tensile strength	3-5 MPa
C	Cohesion	3-10 MPa
ϕ	Friction angle	-
φ	Effective Friction angle	0-20°
ψ	Dilatation angle	0°
f_s, f_t	Yield functions for shear and tensile failure	
$\dot{\lambda}_s$, $\dot{\lambda}_t$	Plastic strain potentials multipliers	
g_s,g_t	Plastic potentials	
DP	Imposed pressure at source walls	
σ	Stress tensor	
ε	Total strain tensor	
p	Mean stress (1st invariant of the stress tensor)	
$\mathbf{s}$	Deviatoric Stress tensor	
$J_2(\sigma)$	2nd Invariant of the deviatoric Shear Stress	
$J_2(\varepsilon)$	2nd Invariant of the deviatoric strain tensor	
$I_1(\varepsilon)$	1st Invariant of the deviatoric strain tensor	
ε_p	Effective plastic strain (2nd invariant of the plastic strain tensor)	

Appendix B. Benchmarks for the combined shear and tensile yield criteria

Appendix B.1. Uniaxial traction test

The purpose is to validate the implementation of the numerical stress update on an elementary test. The sample is a cube of side length L whose faces perpendicular to axis Ox are subjected to a constant normal velocity $v_n = v_0/2$ ($v_0 > 0$). All other faces are set free. The strain rate is then uniform and within the small strain assumption ($v_0 t \ll L$) the only non-zero strain and stress components in the elastic regime are

$$\varepsilon_{xx} = \frac{v_0 t}{L}, \quad \varepsilon_{yy} = \varepsilon_{zz} = -\nu \varepsilon_{xx}, \quad \sigma_{xx} = \sigma(t) = E\varepsilon_{xx}$$

where ν is Poisson's coefficient and E is Young's modulus. The duration of the experiment is T ($T \ll L/v_0$). The first and second invariants of $\boldsymbol{\sigma}(t)$ are simply given by:

$$p(t) = \frac{1}{3}\sigma(t), \quad J(t) = \sigma(t).$$

Onset of plastification

Plasticity onset occurs at the time $t_p = \min\{t \geq 0 \mid f_s(\boldsymbol{\sigma}(t)) \times f_t(\boldsymbol{\sigma}(t)) = 0\}$ which is readily found to be

$$t_p = \frac{\sigma_p}{E} \cdot \frac{L}{v_0} \quad \text{with} \quad \sigma_p = \sigma(t_p) = \begin{cases} 3p_t & \text{if } p_t < p_t^*, \\ 3p_t^* & \text{if } p_t^* \leq p_t \leq p_0. \end{cases}$$

where

$$p_t^* = \frac{2\cos\varphi}{3 + \sin\varphi} c.$$

In other words, failure will occur in shear mode if the tensile strength is greater than p_t^*, in tensile mode if it is smaller than p_t^*, and in mixed tensile and shear mode if it is equal to p_t^*.

Numerical Results

The tests are carried out with the following fixed parameters: $L = 1$ m, $v_0 = 1$ m/s, $E = 10^{11}$ Pa, $\nu = 0.25$, $c = 10^7$ Pa, $\psi = 0°$ and $\varphi = 30°$. Then $p_0 = \sqrt{3}\, c$ and $p_t^* = \frac{2}{7}\, p_0$. Four values of the tensile strength p_t are considered:

$$p_t \in \{\ p_0,\ \ 2 \times p_t^*,\ \ 1 \times p_t^*,\ \ 0.5 \times p_t^*\ \}\,.$$

For the first three tests ($p_t \geq p_t^*$) we must obtain

$$t_p = t_{p,1} := \frac{3p_t^*}{E} = \frac{6\sqrt{3}}{7} \times 10^{-4}\ \text{s}$$

while for the last test ($p_t = p_t^*/2$) we must obtain

$$t_p = t_{p,2} := \frac{3p_t}{E} = \frac{t_{p,1}}{2}.$$

The total duration of the numerical experiment is set to $T = 2t_{p,1}$. Although the mesh size does not matter (strain is uniform) we nevertheless conducted tests with two meshes: a coarse one with 8 nodes and 6 tetrahedrons and a fine one with ca. 1700 nodes and ca. 8000 tetrahedrons. Both give the expected values of t_p and σ_p. Figure (B.1) displays the resulting stress-strain curves and the loading paths in the (p, J) plane.

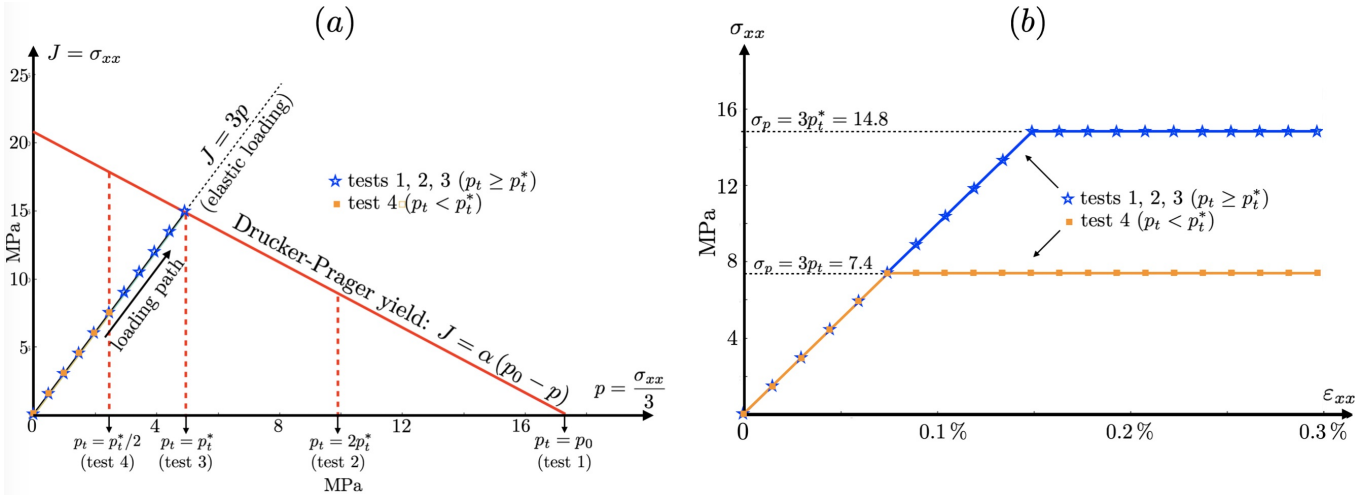

Figure B.1: Test 1 – Uniaxial traction. The loading path (similar color dots) reaches the plastic yielding analytical solutions (plain lines). (a) In the p–J plane and (b) in the $(\sigma_{xx}, \varepsilon_{xx})$ space, for the four different test cases $p_t \in \{ p_0,\ 2 \times p_t^*,\ p_t^*,\ 0.5 \times p_t^* \}$.

Appendix B.2. Compression of a plate with a circular hole

This test is well known in metal engineering, and details can be found in several books (eg. Nádai (1963)). A rectangular plate with a notch is compressed or extended in one direction. With increasing shortening, tensile cracking can occur in the direction parallel to compression while inclined plastic shear bands develop, ultimately breaking the sample in two. Analytical expressions of the elastic stresses are function of the imposed stress σ_∞, the hole's radius a, coordinate r and angle θ that originates parallel to the loading direction (eg. Jaeger and Cook, 1979):

$$\begin{aligned}
\sigma_{rr} &= \tfrac{\sigma_\infty}{2}(1 - \tfrac{a^2}{r^2}) + \tfrac{\sigma_\infty}{2}(1 - \tfrac{3a^4}{r^4} - \tfrac{4a^2}{r^2})\cos(2\theta) \\
\sigma_{\theta\theta} &= \tfrac{\sigma_\infty}{2}(1 + \tfrac{a^2}{r^2}) - \tfrac{\sigma_\infty}{2}(1 - \tfrac{3a^4}{r^4})\cos(2\theta) \\
\sigma_{r\theta} &= -\tfrac{\sigma_\infty}{2}(1 - \tfrac{3a^4}{r^4} + \tfrac{2a^2}{r^2})\sin(2\theta),
\end{aligned} \tag{B.1}$$

Fig.B.2b represents isocontours of the shear stress in case of an applied horizontal traction. Despite a switch in signs these isocontours geometries are similar when exerting a vertical compression. Along the hole's edge in $\theta = 0$ (parallel to the z axis), the radial stress σ_{rr} is null while the tangential stress $\sigma_{\theta\theta}$ becomes equal to $-\sigma_\infty$. In turn in $\theta = \pi/2$ (along the horizontal axis), the radial stress remains null while $\sigma_{\theta\theta}$ reaches $3\sigma_\infty$. Hence, tangential extension occurs at the hole's apex and a crack may appear if the tensile yield is reached there. In turn maximum shear stress develops along the horizontal direction where shear failure will then tend to initiate instead.

We consider here a rectangular plate of size $2\ell_x \times 2\ell_z = 20$ mm $\times$ 36 mm with an inner circular hole of radius $a = 5$ mm, that is compressed at a constant velocity of $v_z = -0.1$ mm/s during 0.3 s. Since the problem is symmetrical, only a quarter of the model domain is considered (cf. Figure B.3a). The material properties are the following : $E = 10^{11}$ Pa, $\nu = 0.25$, $\varphi = 30°$, $\psi = 0°$, $c = 10$ MPa and $p_t = c/10$. As a result, a tensile stress σ_{xx} develops at the hole's apex. With increasing shortening, tensile yield is reached at this location, while a plastic shear band develops at an angle of ca. 60° to the x-direction (Fig. B.3).

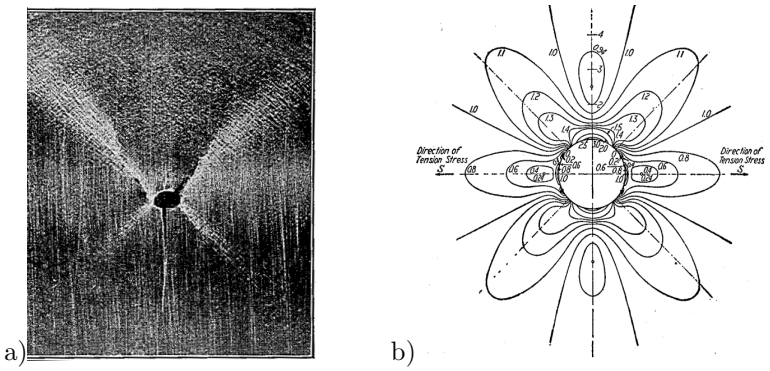

Figure B.2: a) Compression test with a paraffin plate containing a cylindrical hole, and formation of two distinct slip layers departing from the hole . b) Shear stress isocontour lines from equations B.1, for a horizontally stretched elastic plate (opposite stress input). Note the factor 3 concentration at the hole's bottom and apex ($\theta = \pm\pi/2$). After Nádai (1963) (p.286-289).

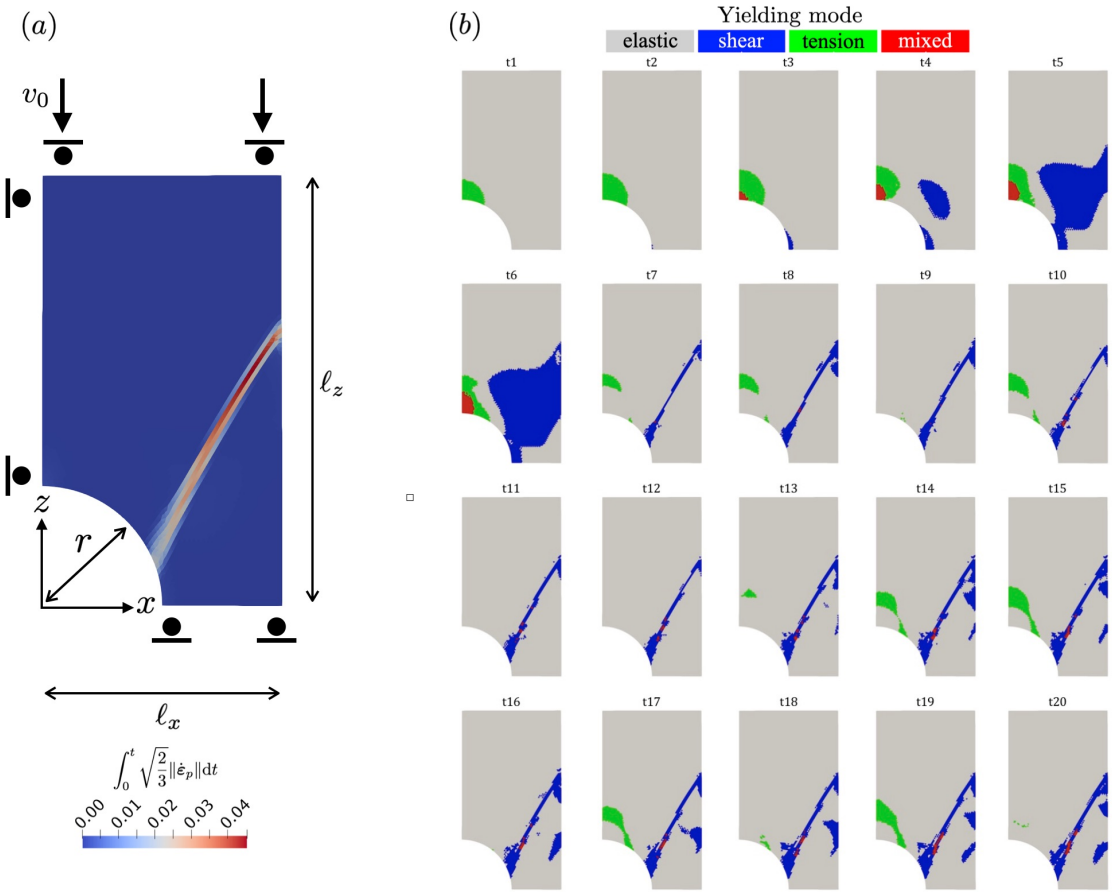

Figure B.3: Test 2 – Compression of a pierced plate. a) set up and accumultated plastic deformation after a nominal shortening of 0.16%. b) 20 snap-shots during loading illustrate the development of the four deformation modes: elastic, plastic shear mode, plastic tensile mode, and mixed tensile and shear mode.

Appendix C. Complementary figures for various model cases

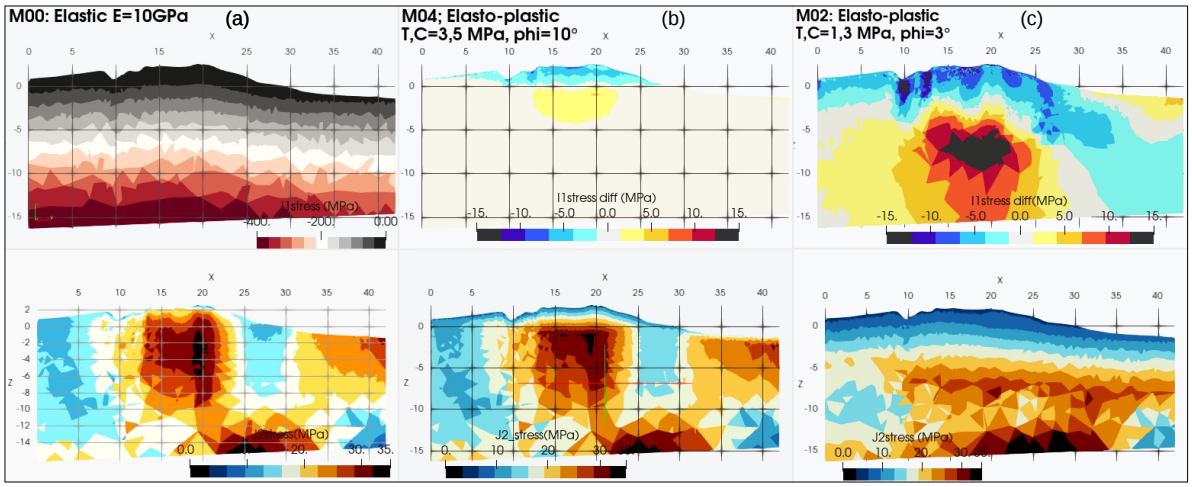

Figure C.1: Stress field with gravity and no magma inflation, in a vertical section along axis $Y = 25.8$ km in models M00 (a), M04 (b) and M02 (c). Top row displays the mean stress (I_1), full values plotted for the elastic case M00 (a), and the differential with respect to this elastic state for M02 (b, $\varphi = 10°$) and M04 (c, $\varphi = 3°$). Plots indicate changes of ± 5 MPa and ± 15 MPa for M04 and M02, respectively, due to plastic yielding above a certain depth. Bottom row displays the deviatoric stress J_2t: he first 2 km in M04 (b) and 5 km in M02 (c) are "cut off" by plastic behavior.

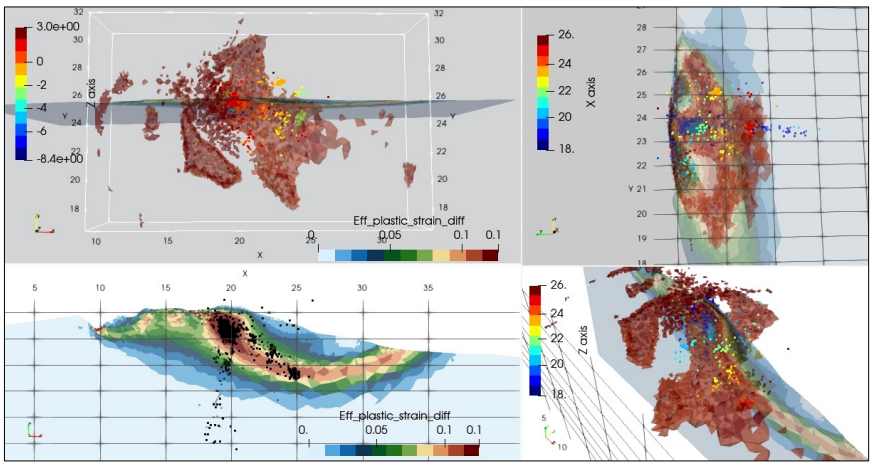

Figure C.2: Comparison of the listric shear zone formed in model M01 with the observed cup-shape seismicity.

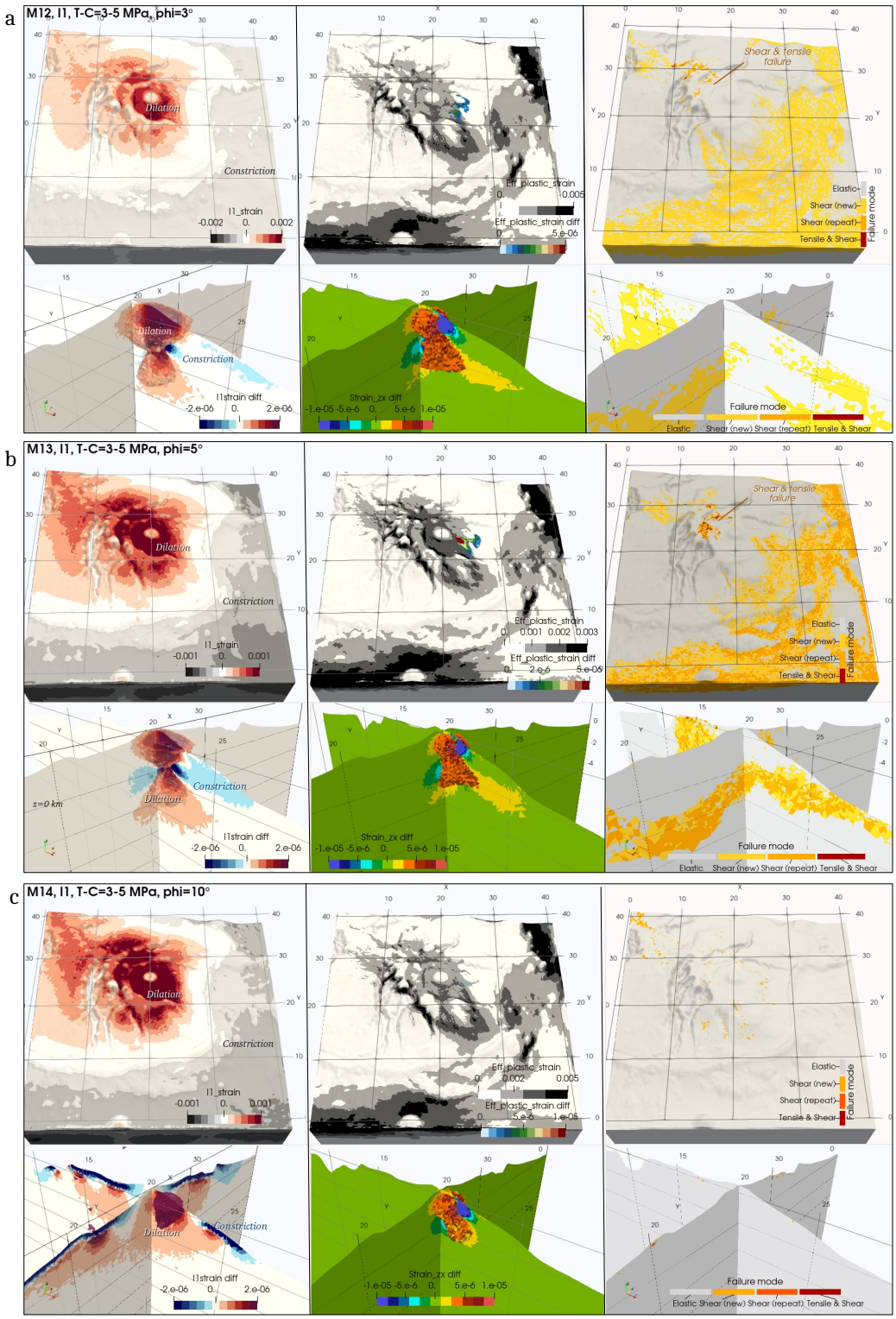

Figure C.3: Complementary figures for models of a dike-like injection (I1).: a) M12, b) M13, c) M14, with 3D top views and 2D vertical sections along Y=25.8 km and X= 20 km. Left : the trace of the strain tensor (dilatation in red, constriction in black or blue), with total values (top) and differential values (bottom). Middle-top : both the total (grey color palette) and the plastic shear strains. Middle-bottom: the differential zx shear strain component, with 3D threshold at $\geq 2.10^{-6}$. Right: shear and tensile failure modes, indicating tensile failure only to the west of the Enclos Fouqué when $\varphi \leq 5°$.

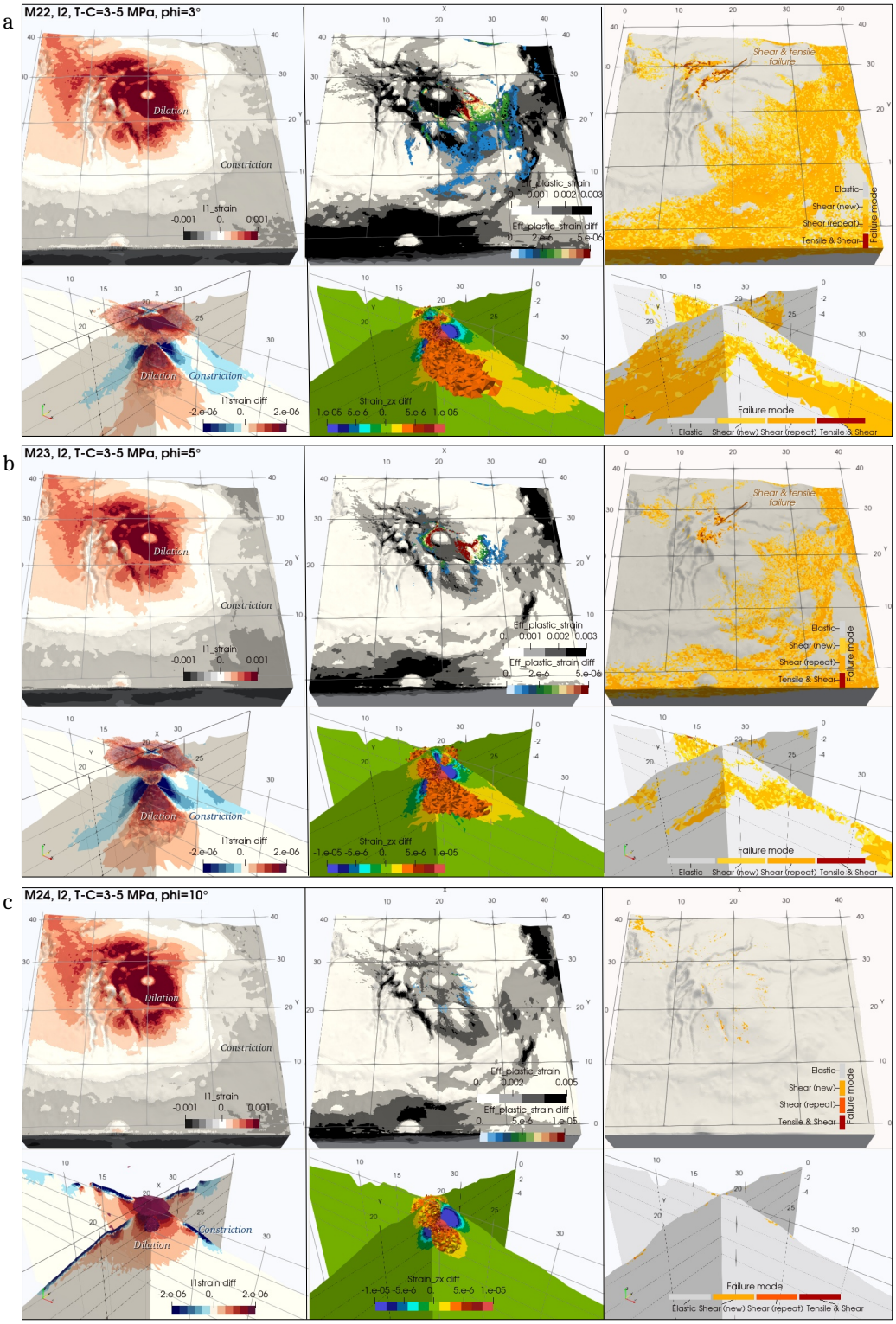

Figure C.4: Complementary figures for models of magmatic reservoir inflation (I2): a) M22, b) M23, c) M24, with 3D top views and 2D vertical sections along Y=25.8 km and X= 19.5 km. Left : the trace of the strain tensor (dilatation in red, constriction in black or blue), with total values (top) and differential values (bottom). Middle-top : both the total (grey color palette) and the plastic shear strains. Middle-bottom: the differential zx shear strain component, with 3D threshold at $\geq 3.10^{-6}$. Right: shear and tensile failure modes, indicating tensile failure only to the west of the Enclos Fouqué when $\varphi \leq 5°$.

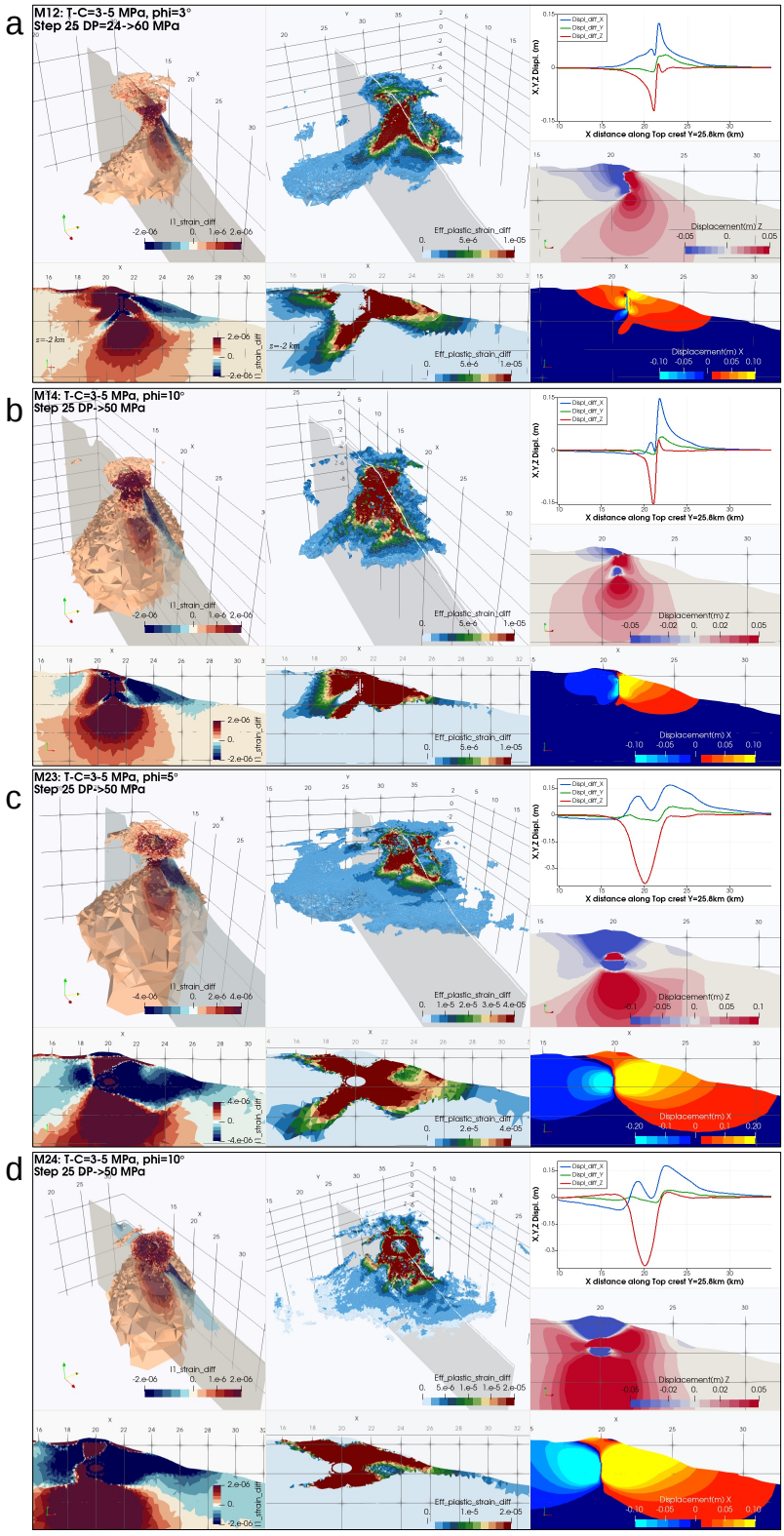

Figure C.5: Models with an overpressure $DP = 50$ MPa at the walls of a distal dike (I1, a-b) and of the magma reservoir (I2, c-d). Left: differential mean strain (dilatation in red). Middle: differential plastic shear strain. Right: displacements. Surface displacements reach 10-20 cm, the strain structures developed at $DP = 10$ MPa remain and no catastrophic flank slide occurs.

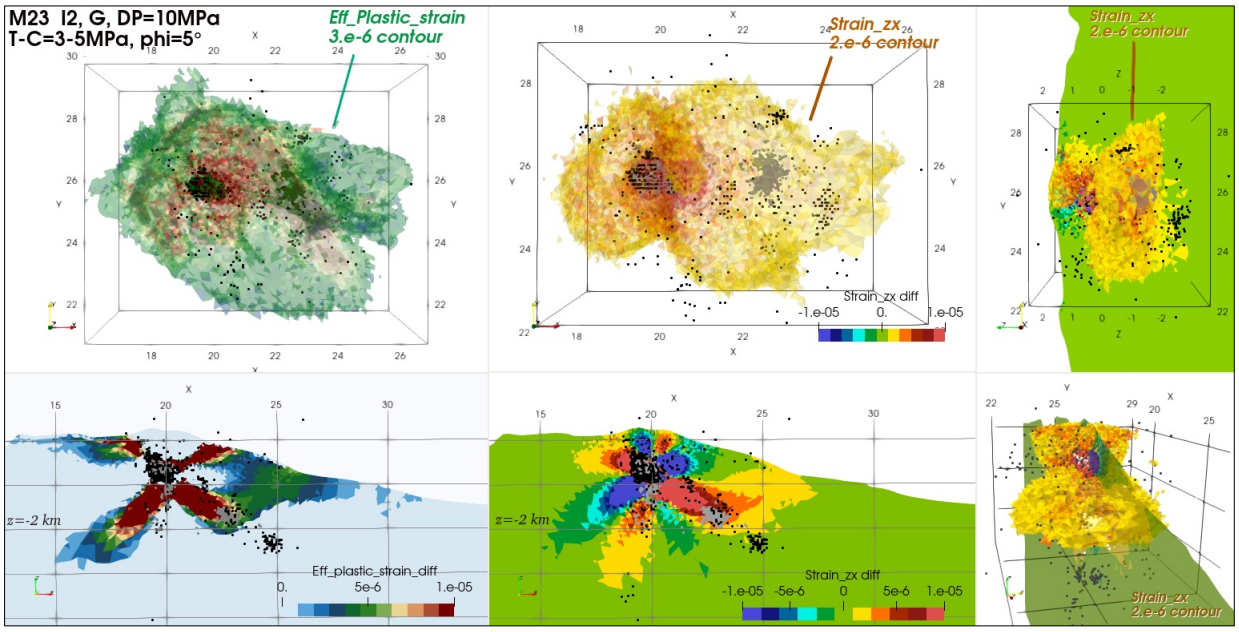

Figure C.6: Comparison of the observed cup-shape seismicity with the shear strain obtained in Model M23 with friction $\varphi = 5°$. The shear zone remains above the seismicity pattern, indicating that this area is still too strong in the models to reproduce observations.

Appendix D. Other Piton de la Fournaise related data

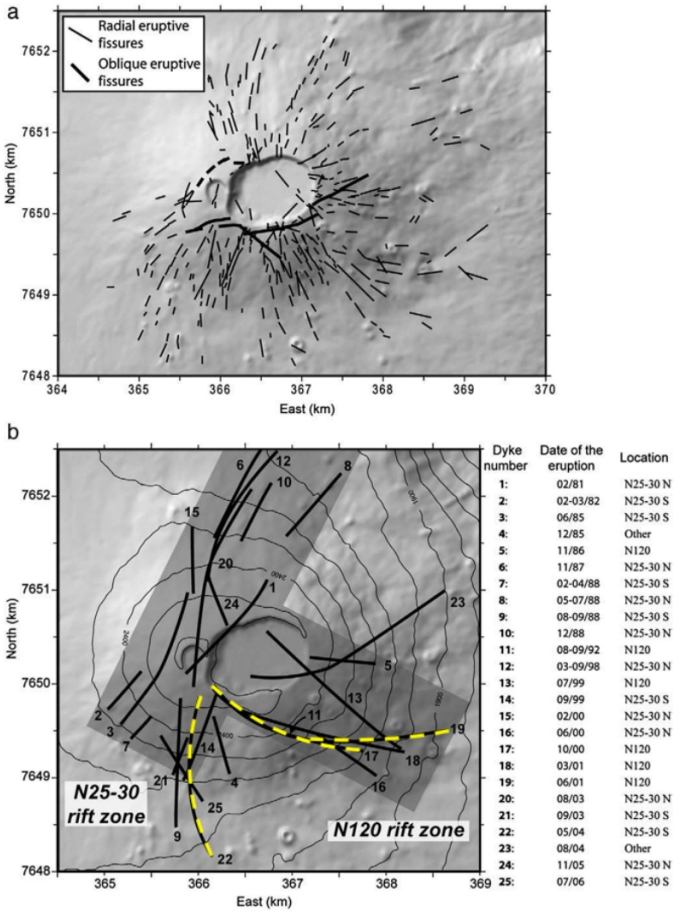

a)

Figure D.1: Mapped structures at Piton de la Fournaise, after Michon et al. (2009): a) Eruptive fissures, b) Dike locations associated to proximal eruptions since 1981 (UTM WGS84 coords.). Note shapes of n°17, 19, 22, comparable to the models.

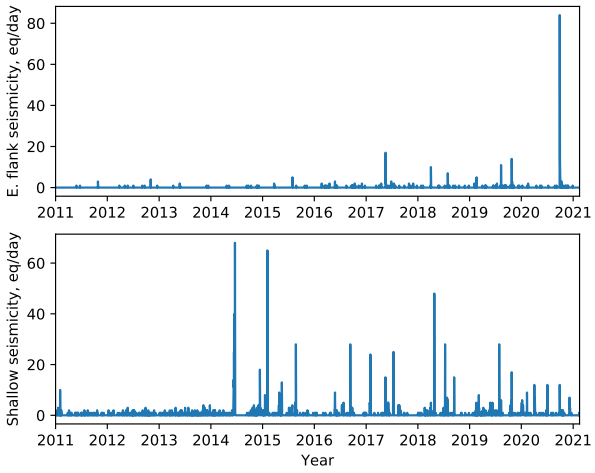

b)

Figure D.2: Seismic activity recorded since 2011 under the Eastern flank and above sea level (source: OVPF).

Appendix E. Alternative models

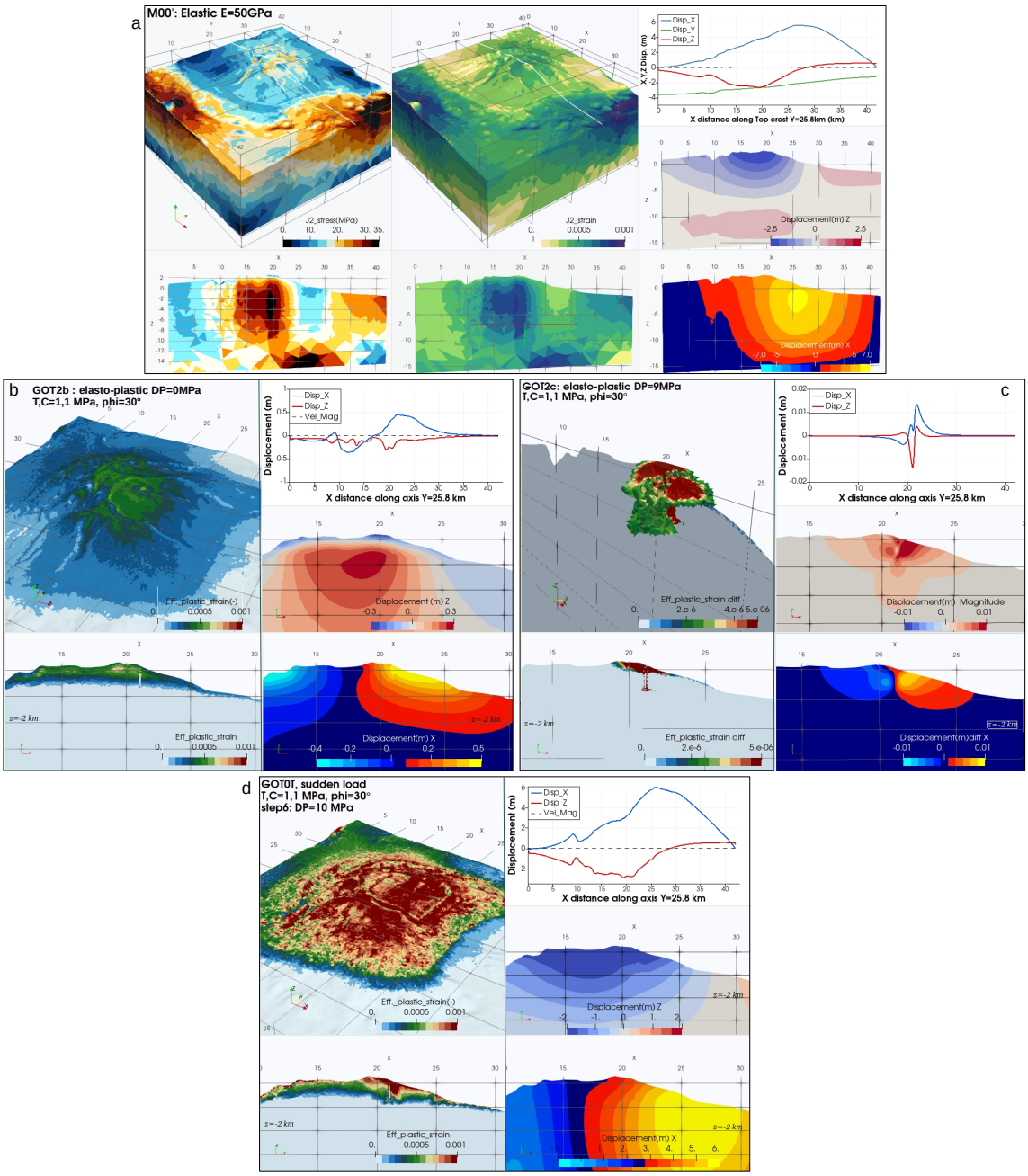

Figure E.1: Inflation of a dike (I1) with parameters similar to those of Got et al. (2013): $E = 50$ GPa, $T = C = 1$ MPa, $\varphi = 30°$, in 3 stages: **a)** the elastic pre-inflation stage (legend as Fig. 5), shows ~ 6 m of displacements. **b)** The elasto-plastic pre-inflation stage produces additional displacements ~ 50 cm. Left: plastic strain, and right: displacement patterns. **c)** Dike inflation up to $DP = 10$ MPa, produces displacements ~ 1 cm. **d)** Alternative model in which dike inflation is applied directly (no pre-inflation stage): note the similar surface displacements to case a).

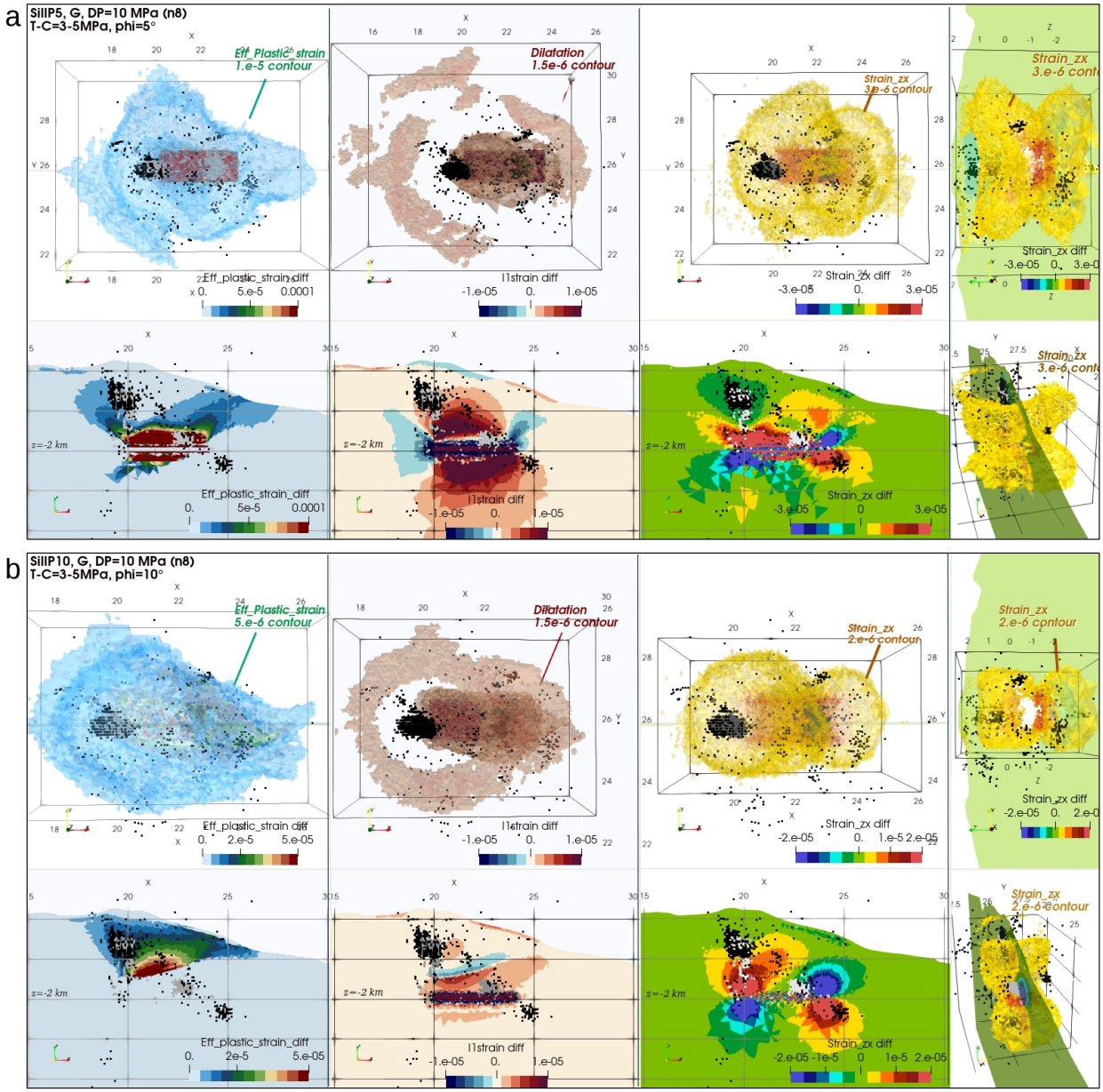

Figure E.2: Inflation of a sill, located at $z = -2$ km depth, departing from below the summit ($X = 20$ km and extending for 4 km eastward. Results are for a friction angle $\varphi = 5°$ (**a**) and $\varphi = 10°$ (**b**). From left to right, the plastic shear strain, the mean strain, and the xz strain component, respectively (differentials from the pre-inflation stage). Upper row displays 3D view from above, lower row displays a vertical section along $Y = 25.8$ km. Superposition of the seismicity cross-cuts the different patterns, and does not provide a clear relationship in either case.